NASA SP-3024

MODELS OF THE TRAPPED RADIATION ENVIRONMENT

Volume I: Inner Zone

Protons and Electrons

JAMES I. VETTE
Aerospace Corporation

A study sponsored by the National Aeronautics and Space Administration and the United States Air Force and prepared under Air Force contract by Aerospace Corporation, El Segundo, California.

Scientific and Technical Information Division 1966
NATIONAL AERONAUTICS AND SPACE ADMINISTRATION
Washington, D.C.

PREFACE

Space systems planners—space engineers as well as physicists—require for their work accurate values of the fluxes and energy spectra of protons and electrons trapped in the geomagnetic field. Numerous measurements have been made of the Van Allen belt radiations on many satellites, with different instruments and at different times. Most of the experimenters organize their data in terms of McIlwain's B, L coordinates, but intercomparison of the results from different experiments is still complicated by temporal variations of the fluxes and differences in energy response of the various instruments used to obtain the data. A need existed, therefore, for collating the individual measurements and for constructing a model environment.

A program, sponsored jointly by the National Aeronautics and Space Administration (Defense Purchase Request W-11, 683) and the United States Air Force (Contract AF 04(695)-469) is in progress under the direction of Dr. Vette for the express purpose of constructing such a model environment. This report contains a description of the model which has been developed for the inner radiation belt. The graphs in this report give a picture of the radiations; card decks containing the actual flux values have also been prepared and can be used in subroutines of larger computer programs. In addition, codes have been developed for integrating the flux along satellite orbits. Persons on NASA sponsored projects may request such integrations from Wilmont N. Hess, Goddard Space Flight Center, and those on Air Force projects should request it from James I. Vette, Aerospace Corporation.

As this effort continues, major emphasis will be placed on describing the outer radiation belt, updating the model of the inner belt, and developing the capability to predict changes that are likely to occur in the particle populations. Hopefully, such changes can be correlated with geophysical indicators or other events.

This effort would not be possible without the assistance given to this project by the experimenters who made the measurements originally. All users of this environment will greatly appreciate these efforts. It is to be hoped that this original enthusiasm will continue and permit us to maintain an up-to-date model environment.

A. W. Schardt
Physics & Astronomy Programs
NASA Headquarters

CONTENTS

INTRODUCTION

For 16 months we have been engaged in a NASA/Air Force supported program to produce trapped radiation model environments that will be of general use to space engineers, systems planners, and space physicists. An outline of this effort has been described previously (Reference 1) and several model environments for the inner zone have been distributed. The present report will provide (1) more details concerning the production of these environments and (2) a detailed comparison with the existing satellite data.

It is necessary to combine data from many satellites in order to obtain a good over-all picture of the trapped radiation. Furthermore, the inclusion of newer data at regular intervals is mandatory because our knowledge of the radiation belts increases as improved instruments are flown and new ideas are advanced. The appropriate time scale for updating still seems to us to be about six months. However, during the initial phase of the present program a longer period of time has been required to collect the data, assess them, and produce an output. The inner zone electron map AE1 was completed after eight months and the proton maps AP1 through AP4 required an additional eight months. However, various procedures had to be learned, computer programs had to be developed, and personnel had to be acquired during this period. It is felt that future environments can be produced more rapidly and detailed descriptive reports such as this can follow closely the initial distribution of the flux maps.

GENERAL PROCEDURE

The three quantities that need to be determined by comparing data from various sources are the flux distribution, the energy spectrum, and the absolute value. In general, the flux is a function of particle energy, time, position, and magnetic or solar activity. A detailed representation in all of these variables would not be very practical because it would be too cumbersome to use. Emphasis has been placed on dividing the environment into various segments of space, energy, and time so that simplifications of representation and use can be achieved.

We have started by analyzing the inner zone radiations first for the following reasons. The most intense regions of trapped radiation exist there, many satellite programs are concerned with the proper design to function reliably in these radiations, and our knowledge of this region is more complete. Over much of the inner zone the B, L coordinate system offers a good way to present the data. The general variations are long term decay or growth with characteristic times of months and years out to $L \approx 2.0$; at larger values definite responses to magnetic activities are observed, and changes are produced in much shorter times.

At present, data are received in reports or private communications in a wide variety of formats. Omnidirectional measurements above a certain energy or within a given energy band are common. More recently, unidirectional fluxes perpendicular to the magnetic field line, $j_\perp$, have been measured by instruments on Injun III, Relay I, and Relay II. Other directional data are given in terms of equatorial or local pitch angle distributions. Within this framework of measurements the data are presented in many ways and coordinate systems such as:

1. B-L flux maps
2. R-λ flux maps
3. Flux-B maps
4. Flux-x maps
5. Flux-B/B_0 maps
6. Local pitch angle distributions
7. Equatorial pitch angle distributions

We have chosen to convert all of these into one common format which can be stored on punched cards for further processing and for comparison. For the inner zone data, which we consider below $L = 3.0$, we have found the most useful format to be omnidirectional flux plotted versus B. Thus all data received is converted to omnidirectional flux. A series of values of flux, F, and B for a given L value are punched on cards; enough points are used so that values at other B points can be obtained by interpolation. The L values

$$L_i = 1.1 + 0.1i ; \qquad (i = 1, 2, \cdots 19)$$

have been chosen as a compromise between processing too much data and obtaining poor interpolations at intermediate L values. As the techniques become more automated, a finer L grid will become feasible.

Hopefully in the future, data can be provided to us in formats which are easy to handle or will be provided on punched cards in our standard format. Such a procedure would result in a considerable saving of time and the lag between receipt of data and production of the environment would be minimized.

If spectral measurements are available, then a model spectrum can be devised. On the basis of this spectrum, all the measurements are converted to a common energy and a detailed comparison results in the selection of the B dependence of the flux. However, the spectrum may have to be obtained by an iteration with selected measurements. Comparison with other data can be done to determine the feasibility of the model. After the flux-B curves are drawn, a B-L flux map is constructed by cross plotting. This presentation is very useful in showing some of the inconsistencies that developed in selecting the B dependence. An iteration between the B-L map and the F-B plot generally produces a smooth representation in both systems that is consistent with the data. R-λ maps and equatorial pitch angle distributions are constructed from the resulting model by further calculation. Finally the model is read into the computer so that integrations over selected circular orbits can be performed in a manner in which the spectral information is preserved.

In the following sections these general procedures will be described in more detail and the model environments will be compared with the data used in making them.

OMNIDIRECTIONAL - UNIDIRECTIONAL FLUX CONVERSIONS

Since a large amount of input data was received as perpendicular flux, equatorial or local pitch angle distributions, it was necessary to develop an efficient computer program to convert these data to omnidirectional fluxes. The inverse transformation is also useful in analyzing data and in presenting final results.

The conversion from unidirectional to omnidirectional flux was formulated in a manner very similar to that given recently by Roberts (Reference 2). The omnidirectional flux, J, at a given position on the L shell given by the field strength, B, in terms of the unidirectional flux, j, at that point is

$$J(B, L) = 4\pi \int_0^{\mu_c} j(B, L, \mu)\, d\mu \ , \qquad (1)$$

where

μ = cosine of the local pitch angle

μ_c = cutoff value of μ which defines the loss cone, i.e., $j(B,L,\mu) = 0$ for $\mu \geq \mu_c$.

In terms of Robert's variable

$$x = (1 - B_0/B)^{1/2} \ ,$$

where B_0 is the field strength at the magnetic equator, the mirror equation is written as

$$(1 - x^2)(1 - \mu^2) = (1 - x_1^2)(1 - \mu_1^2) \ . \qquad (2)$$

If one relates the general values x, μ to the equator values by means of (2), then

$$1 - \mu^2 = \frac{1 - y^2}{1 - x^2} \tag{3}$$

where we have written y as the cosine of the equatorial pitch angle. In terms of x and y, (1) becomes

$$J(x) = \frac{4\pi}{\left(1 - x^2\right)^{1/2}} \int_{y=x}^{y_c} \frac{y\, j(y)\, dy}{\left(y^2 - x^2\right)^{1/2}} . \tag{4}$$

We have suppressed the L variable in (4) and write $j(y)$ for the equatorial pitch angle distribution. Of course y_c is the cutoff value defining the loss cone.

The variables x and y cover the range

$$0 \leq x \leq y_c$$

$$0 \leq y \leq y_c$$

which we divide into intervals by means of the points

$$y = 0, y_1, y_2, \cdots y_i \cdots y_n$$

$$x = 0, x_1, x_2, \cdots x_i \cdots x_n$$

with $x_i = y_i$ and $y_n = y_c$. For a given value of $x = x_{k-1}$ we can write (4) as

$$J(x_{k-1}) = \frac{4\pi}{\left(1 - x_{k-1}^2\right)^{1/2}} \sum_{i=k}^{n} \int_{y_{i-1}}^{y_i} \frac{y\, j(y)\, dy}{\left(y^2 - x_{k-1}^2\right)^{1/2}} .$$

If the intervals are taken small enough, j will not vary appreciably over the interval and can be removed from the integral. Then one obtains

$$J(x_{k-1}) = \frac{4\pi}{\left(1 - x_{k-1}^2\right)^{1/2}} \sum_{i=k}^{n} j(\bar{y}_i) \int_{y_{i-1}}^{y_i} \frac{y\, dy}{\left(y^2 - x_{k-1}^2\right)^{1/2}} . \tag{5}$$

The quantity $\bar{y}_i$ is the value of y between y_{i-1} and y_i which is most appropriate to use to evaluate j and will be discussed later. The integral in (5) is trivial and can be done immediately. If we define

$$J_k \quad J(x_{k-1})$$

$$j_i \quad j(y_i)$$

$$A_{ik} \quad \begin{cases} \dfrac{4\pi}{\left(1 - x_{k-1}^2\right)^{1/2}} \left[\left(y_i^2 - x_{k-1}^2\right)^{1/2} - \left(y_{i-1}^2 - x_{k-1}^2\right)^{1/2}\right] ; & i > k \\ 0 ; & i < k \end{cases}$$

we can write (5) as the matrix equation

$$J_k \quad \sum_{i=1}^{n} A_{ik}\, j_i \; .$$

This matrix is similar to that given in Reference 2; however, we have formulated it for unequal intervals because the function $j(y)$ changes rapidly as $y \to y_c$ in many cases and one needs to take small intervals in this region. Although this matrix is independent of L, we have found it necessary to make the spacing, or selection of y_i and x_i, depend on L because the cutoff of the fluxes is L-dependent. We have made 19 differently spaced 45 by 45 triangular matrices to use at the L values 1.2, 1.3 . . . . 3.0 where the various data have been tabulated for the inner zone.

We have determined a value for y_i in the following manner. The first few terms in (5) are the main ones because the integrand is largest for a given interval size and j is generally a monotonically decreasing function of y. For those regions where j varies slowly with y, setting $\bar{y}$ equal to any point in the interval will give nearly the same answer. However where j changes rapidly, the accuracy of this approximate method depends on the choice of y_i. Consider the integral for the first interval

$$I \quad \int_{y=x}^{x+\alpha} \frac{j(y)\, y\, dy}{\left(y^2 - x^2\right)^{1/2}}$$

and define y_1 by the equation

$$j(y_1)\left[(x + \alpha)^2 - x^2\right]^{1/2} \qquad I \; .$$

We expand $j(y)$ in a Taylor series about x and substitute into the integral to obtain

$$j(y_1) \quad j(x) + j'(x)\left\{\frac{\alpha}{2} - \frac{x}{2} + \frac{x^2}{2\left(2x\alpha + \alpha^2\right)^{1/2}} \log\left[1 + \frac{\alpha + \left(2\alpha x + \alpha^2\right)^{1/2}}{x}\right]\right\} + \text{higher order terms in } \alpha.$$

To first order we see

$$\bar{y}_1 = \frac{1}{2}\left\{\alpha + x + \frac{x^2}{\left(2x\alpha + \alpha^2\right)^{1/2}} \log\left[1 + \frac{\alpha + \left(2x\alpha + \alpha^2\right)^{1/2}}{x}\right]\right\} \qquad (6)$$

We have used (6) to determine the evaluation point for all the intervals, namely

$$\bar{y}_i = \frac{y_i}{2} + \frac{y_{i-1}^2}{2\left[y_i^2 - y_{i-1}^2\right]^{1/2}} \log\left[1 + \frac{\left(y_i - y_{i-1}\right) + \left(y_i^2 - y_{i-1}^2\right)^{1/2}}{y_{i-1}}\right]. \qquad (7)$$

The required vector j_i at the selected points given by (7) can be interpolated from an input tabular function representing the equatorial pitch angle distribution or the unidirectional flux perpendicular to the field line, $j_\perp$. If x_m represents the mirror point value for a particle whose equatorial pitch angle cosine is y, then Liouville's theorem states that

$$j(y) = j_\perp\left(x_m\right).$$

From this it is seen that these two forms of input are handled in exactly the same way.

The inverse matrix method of Reference 2 was not used for the L region below 3.0 to convert omnidirectional flux into unidirectional because the results with tabular inputs produced some bumps particularly where the spacing interval $y_i - y_{i-1}$ changed. In general this results because the slope of the input function is very important in the calculation. However, the continuity of this slope is not usually watched very closely when one is reading points off a graph, especially with a logarithmic scale. To understand the importance of the derivative, we have formulated the conversion in a different manner. The integral expression that relates J to j has been given by several authors (References 2, 3, and 4). We started with the expression given by Farley and Sanders (Reference 4).

$$j = \frac{-B_m^{3/2}}{2\pi^2} \int_{B_m}^{B_c} \frac{dB}{\left(B - B_m\right)^{1/2}} \frac{d}{dB}\left(\frac{J}{B}\right)$$

and using the equations

$$B = \frac{B_0}{1 - x^2}$$

$$B_m = \frac{B_0}{1 - y^2}$$

$$B_c = \frac{B_0}{1 - x_c^2} = \frac{B_0}{1 - y_c^2},$$

have obtained

$$j(y) = -\frac{1}{2\pi^2\left(1-y^2\right)}\int_y^{y_c} \frac{\left(1-x^2\right)^{1/2}}{\left(x^2-y^2\right)^{1/2}} \frac{d}{dx}\left[\left(1-x^2\right)J\right] dx \; . \tag{8}$$

The simpler expression given by Roberts (Reference 2)

$$j(y) = -\frac{1}{2\pi^2}\int_{x=y}^{y_c} \frac{1}{\left(x^2-y^2\right)^{1/2}} \frac{d}{dx}\left[\left(1-x^2\right)^{1/2} J\right] dx \tag{9}$$

can be integrated by parts to show that (8) and (9) are equivalent.

By breaking up the x and y range into intervals, as has been discussed previously, one can write (8) as

$$2\pi\left(1-y_{k-1}^2\right)^{1/2} j\left(y_{k-1}\right) = -\sum_{i=k}^{N}\int_{x_{i-1}}^{x_i} \frac{\left(1-x^2\right)^{1/2}}{\left(x^2-y_{k-1}^2\right)^{1/2}} \frac{d}{dx}\left[\left(1-x^2\right)J\right] dx \; . \tag{10}$$

The assumption that $J(x)$ can be approximated over the ith interval by

$$J_i(x) = c_i\, e^{-B/b_i} = c_i\, e^{-B_0/b_i\left(1-x^2\right)} \tag{11}$$

is known to be reasonable because all the data are plotted before input to the computer is made. Enough points are fed in to make interpolation in this form valid. Here c_i and b_i are constant over the interval. Differentiating (11) with respect to x and substituting into (10), we find

$$2\pi^2\left(1-y_{k-1}^2\right) j\left(y_{k-1}\right) =$$

$$\sum_{i=k}^{N}\int_{x_{i-1}}^{x_i} J_i(x)\left[\frac{2x\left(1-x^2\right)^{1/2}}{\left(x^2-y_{k-1}^2\right)^{1/2}} + \frac{2xB_0}{b_i\left(1-x^2\right)^{1/2}\left(x^2-y_{k-1}^2\right)^{1/2}}\right] dx \; . \tag{12}$$

Again if the intervals are small enough, $J_i(x)$ can be removed from the integral. We have defined the D and E matrices by

$$D_{ik} \equiv \begin{cases} \dfrac{1}{2\pi^2\left(1-y_{k-1}^2\right)}\displaystyle\int_{x_{i-1}}^{x_i} \frac{2x\left(1-x^2\right)^{1/2}}{\left(x^2-y_{k-1}^2\right)^{1/2}}\, dx \; ; & i \geq k \\[2ex] 0 \; ; & i < k \end{cases}$$

$$E_{ik} \equiv \begin{cases} \dfrac{B_0}{2\pi^2\left(1 - y_{k-1}^2\right)} \displaystyle\int_{x_{i-1}}^{x_i} \dfrac{2x\,dx}{\left(1 - x^2\right)^{1/2}\left(x^2 - y_{k-1}^2\right)^{1/2}} \; ; & i \geq k \\ 0 \; ; & i < k \end{cases}$$

and the vectors

$$F_i \equiv J_i\left(\bar{x}_i\right)$$

$$F_i' \equiv \frac{J_i}{b_i} = \frac{dJ_i}{dB}$$

$$j_k \equiv j\left(y_{k-1}\right) .$$

If these are used, then (12) can be written as the matrix equation

$$j_k = \sum_{i=0}^{N} \left(D_{ik}\,F_i + E_{ik}\,F_i'\right) .$$

Using

$$p = \left(\frac{x_i^2 - y_{k-1}^2}{1 - x_i^2}\right)^{1/2}$$

$$q = \left(\frac{x_{i-1}^2 - y_{k-1}^2}{1 - x_{i-1}^2}\right)^{1/2} ,$$

the matrices can be expressed as

$$D_{ik} = \begin{cases} \dfrac{1}{2\pi^2}\left(\dfrac{p}{p^2 + 1} + \tan^{-1} p - \dfrac{q}{q^2 + 1} - \tan^{-1} q\right) ; & p^2 \geq 0 \\ 0 \; ; & p^2 < 0 \end{cases}$$

$$E_{ik} = \begin{cases} \dfrac{B_0}{\pi^2\left(1 - y_{k-1}^2\right)}\left(\tan^{-1} p - \tan^{-1} q\right) ; & p^2 \geq 0 \\ 0 \; ; & p^2 < 0 . \end{cases}$$

The two matrices were constructed as 45 by 45 triangular ones at each of the L values of interest.

The conversion of flux from one form into the other requires a knowledge of the omnidirectional flux at all points along the field line or of a complete equatorial pitch angle distribution. Most measurements only supply a portion of the required range. The most common case is shown in Figure 1. In order to make the conversion of these data, extrapolated data shown by dotted lines are also fed into the computer. The computer is made to calculate separately for the real data and extrapolated data. If the converted flux is composed of more than 75% real data, it is treated as real data in the new form; otherwise it is treated as extrapolated data.

All of the flux data below $L = 3.0$ have been converted by this program so that $J(B, L)$ and $j_\perp(B, L)$ exist on punched cards in our standard card format which is explained in the next section.

For arbitrary L values we have employed the method given by Roberts (Reference 2) except that we have made a variable-spaced 45 by 45 matrix

$$a_{ik} = \begin{cases} 4\pi\left[\left(\alpha_i^2 - \beta_{k-1}^2\right)^{1/2} - \left(\alpha_{i-1}^2 - \beta_{k-1}^2\right)^{1/2}\right] & ; \quad i \geq k \\ 0 & ; \quad i < k \end{cases}$$

where

$$\alpha_i y_c = y_i$$

$$\alpha_k y_c = x_k$$

instead of a uniformly spaced one. The omnidirectional flux is obtained from

$$G\left(x_{i-1}\right) = \left(1 - x_{k-1}^2\right)^{1/2} J\left(x_{k-1}\right) = y_c \sum_{i=1}^{45} a_{ik}\, j\left(\bar{y}_i\right)$$

and the unidirectional flux is obtained from

$$j\left(y_{k-1}\right) = \frac{1}{y_c} \sum_{i=1}^{45} a_{ik}^{-1}\, G\left(\bar{x}_i\right)$$

where a_{ik}^{-1} is the inverse matrix of a_{ik}.

PUNCHED CARD FORMAT

We will describe the format we have chosen to store the trapped radiation data on punched cards since others may wish to use these cards. A given set of cards containing the data function

$F(B, L)$ is comprised of a partitioned subset of cards; each subset corresponds to a fixed L value. At the head of each subset there is a header or title card followed by the data cards for that L value. Thus an entire deck of cards covering all L values is ordered so that the first card is a header card which is followed by its data cards; then the same sequence is repeated at each L value. The formats of the header card and data card are given below.

Header Card Format

Columns 1 - 60	Used to describe the data in alpha numeric symbols.
Columns 61 - 66	Not used at present.
Column 67	A zero (0) indicates that the data does not cover the whole range of B values. A one (1) indicates a complete set of data which spans from the equator to the atmospheric cutoff.
Columns 68 - 69	Give the number of data cards behind the header card.
Column 70	Not used.
Column 71	Denotes the type of data with the following code: 0 - Extrapolated data 1 - Omnidirectional flux 2 - Unidirectional flux 3 - Unidirectional flux perpendicular to field line, $j_{\perp}$ 4 - Counting rate, omnidirectional 5 - Counting rate, unidirectional 6 - Counting rate, perpendicular 7 - Composite environment, omnidirectional flux 8 - Composite environment, unidirectional flux 9 - Other The composite environment refers to those produced in this program such as AE1, AP1, etc.
Column 72	Denotes the particle and approximate energy threshold with the following code: 0 - Protons < 0.1 MeV 1 - Protons 0.1 - 1.0 MeV 2 - Protons 1 - 4 MeV 3 - Protons 4 - 30 MeV 4 - Protons >30 MeV 5 - Electrons <30 keV 6 - Electrons 30 - 300 keV 7 - Electrons 0.3 - 1.0 MeV 8 - Electrons >1.0 MeV 9 - Unspecified at present

Columns 73 - 75	Identification of the source of the data. The first digit gives the experimental group or groups and the last two digits will index their data. The code for the experimental groups is: 000 - 099 - Aerospace Corporation 100 - 199 - Air Force Cambridge Research Laboratory 200 - 299 - Bell Telephone Laboratories 300 - 399 - Goddard Space Flight Center 400 - 499 - Lockheed Missile and Space Company 500 - 599 - University of California at San Diego 600 - 699 - State University of Iowa 700 - 749 - Applied Physics Laboratory, Johns Hopkins University 750 - 799 - Rice University 800 - 899 - Composite environment 900 - 949 - University of Minnesota 950 - 999 - University of California (including Lawrence Radiation Laboratory) Of course as other groups begin to contribute data, new assignments of numbers will be made.
Columns 76 - 79	Give the L value as x.x.
Column 80	Not used.

An example of a header card is shown in Figure 2.

Data Card Format

Columns 1 - 60	Contain four pairs of values of the form (B, F) for a fixed L value. Each pair has a field of fifteen columns; the first six columns are for B and the last nine are for F. The format B is xxxxx and the format for F is either .xxxEyy or .xxxE+yy. The exponent is understood to be positive when it is not punched.
Columns 61 - 70	Not used at present.
Columns 71 - 78	Are same as header card.
Columns 79 - 80	Used for indexing the data cards behind the header card.

Two examples of data cards are shown in Figure 2.

ENERGY SPECTRUM

We have found it useful to represent the differential energy omnidirectional flux, J(E, B, L), as a product of two functions

$$J(E, B, L) = F(B, L)\left[\frac{n(E, B, L)}{\int_{E_1}^{\infty} n(E', B, L)\, dE'}\right] . \qquad (13)$$

We call $F(B, L)$ the distribution function and the term in the brackets is the differential spectrum normalized such that the integral spectrum

$$N(>E, B, L) = \int_E^{\infty} N(E', B, L)\, dE' = \frac{\int_E^{\infty} n(E', B, L)\, dE'}{\int_{E_1}^{\infty} n(E', B, L)\, dE'}$$

is equal to 1 for $E = E_1$. We will suppress the B and L variables and write $N(E, E_1)$ for the differential spectrum and $N(>E, E_1)$ for the integral spectrum normalized in this manner. Using (13) and this notation, the integral energy omnidirectional flux is written as

$$J(>E, B, L) = F(B, L)\, N(>E, E_1)$$

and we see that the distribution function represents the flux above energy E_1.

Because measurements are made with instruments of different spectral characteristics, it is imperative to have some knowledge of the energy spectrum in order to compare different sets of data. One is either provided with some direct spectral measurements or can obtain this information by an iterative process with several sets of data if the spectral characteristics of the various instruments are known. To illustrate the importance of this spectral information in making model environments, we will discuss the common threshold detector which has supplied much of the trapped radiation data.

The efficiency versus energy curves for two of the electron detectors flown on Relay I are given in Figure 3 (References 5 and 6). Although these two detectors were actually directional ones, we will proceed with the discussion in omnidirectional form. The observational quantity of such a device is the counting rate, c, which is converted into a flux by the relationship

$$F(B, L) = \frac{c(B, L)}{G \int_0^{\infty} \epsilon(E)\, N(E, E_1)\, dE} .$$

Here G is the geometrical factor and we have expressed all of the energy dependence of the detector in the $\epsilon(E)$ term. In order to understand more fully the limitations of the threshold detector, we consider the idealized efficiency curve given in Figure 4 and assume an exponential spectrum

$$N(E, E_T) = \frac{\exp\left(\frac{E_T - E}{E_0}\right)}{E_0}$$

which is normalized in our usual way at E_T. It is easy to show that average efficiency

$$\bar{\epsilon} = \int_0^\infty \epsilon(E)\, N(E, E_T)\, dE = \epsilon_0 \frac{E_0}{\Delta} \sinh \frac{\Delta}{E_0}$$

in this case. We see that

$$\bar{\epsilon} = \epsilon_0 \left[1 + \frac{1}{6}\left(\frac{\Delta}{E_0}\right)^2\right] \quad \text{for} \quad \frac{\Delta}{E_0} \ll 1 .$$

For this example $\bar{\epsilon}$ is constant to second order and the detector is insensitive to spectral changes. It is interesting to note that had we chosen to call the threshold energy of this idealized detector $E_T \pm \Delta$, then the average efficiency would be

$$\bar{\epsilon} = \epsilon_0 e^{\pm\Delta/E_0} \frac{E_0}{\Delta} \sinh \frac{\Delta}{E_0}$$

or for $\Delta/E_0 \ll 1$,

$$\bar{\epsilon} = \epsilon_0 \left(1 \pm \Delta/E_0\right)$$

which is only constant to first order. Thus it is better to associate the threshold energy of a detector with the approximate mid point of the rising efficiency curve when the spectrum is not accurately known.

If one uses a power law spectrum

$$N(E, E_T) = \left(\frac{E}{E_T}\right)^{-(b+2)} \frac{(b+1)}{E_T} ; \qquad b > 0$$

in the preceding analysis, then

$$\frac{\bar{\epsilon}}{\epsilon_0} = \frac{1}{2\gamma}\left(\frac{b+1}{b}\right)\left[\frac{1}{(1-\gamma)^b} - \frac{1}{(1+\gamma)^b}\right]$$

$$- \frac{1}{2\gamma}\left[\frac{1}{(1-\gamma)^b} - \frac{1-\gamma}{(1+\gamma)^{b+1}}\right] + \frac{1}{(1+\gamma)^{b+1}}$$

where $\gamma = \Delta/E_T$. If $\gamma \ll 1$, then

$$\frac{\bar{\epsilon}}{\epsilon_0} = 1 + \frac{(b+1)(b+2)\gamma^2}{6} .$$

It is apparent that $\epsilon(E)$ must be known for the different measurements in order to obtain a spectrum or to compare the data in detail; unfortunately this information is not always available.

DISTRIBUTION FUNCTION

When a given model spectrum is obtained (by whatever means are available), the various measurements can be converted to some common energy value. The energy value chosen is usually that of some extensive measurement or near several different measurements so that errors in the model spectrum will not produce large errors in converting fluxes to the common energy point. If an experimental measurement of flux above energy E_2 is denoted by

$$J_m\left(>E_2, B, L\right)$$

the quantity

$$F_m(B, L) = \frac{J_m\left(>E_2, B, L\right)}{N\left(>E_2, E_1\right)}$$

represents the data converted to a flux above energy E_1 by the model spectrum. If a measurement covers an energy band $E_2 - E_3$, then the conversion is made by

$$F_m(B, L) = \frac{J_m\left(E_2 - E_3, B, L\right)}{N\left(>E_2, E_1\right) - N\left(>E_3, E_1\right)} .$$

Following this procedure with all the available measurements, one obtains a series of curves at each L value. Some type of mean value is taken from this and becomes the F(B,L) for the model environment. It has been found necessary to draw the B-L flux map presentation in order to draw curves through the scatter of points at each L value in a somewhat consistent fashion. Examples of distribution functions and the converted data used in making them will be shown later in connection with each model environment.

ORBITAL INTEGRATIONS

Having the environment in terms of the spectral and distribution functions is very useful for comparing with new experimental data or for designing space experiments. One of the most useful ways of displaying the data for engineering and planning purposes is by giving the average accumulated flux that a satellite will receive in orbiting the earth. This is generally called the orbital integrated flux and will be denoted by

$$\phi(>E) = \int_0^T \frac{J(>E, B, L)\, dt}{T} .$$

The calculation is performed on a computer using a series of standard subroutines. Many of these have been described elsewhere (Reference 7) so a detailed discussion will not be given here. An orbit program calculates the altitude, latitude, and longitude (h, θ, ϕ) at various times along the orbit. $B(h, \theta, \phi)$ is calculated using the 1960 Jensen and Cain coefficients (Reference 8), and then L is calculated. The flux for this B, L point is then obtained and multiplied by the time interval between successive points. Proceeding in this fashion and accumulating the flux-time interval product, ϕ is obtained. The time intervals used must be small enough so that the integral is adequately done by the trapezoidal rule and the total time, T, should be long enough to obtain the desired average.

Since the manner in which the flux map is interpolated for a given B, L point varies, we will describe how it has been done for the orbital integrations presented later in this work. Flux values are stored for a series of B values at discrete L values. We denote the L values by L_i and order them so that $L_i < L_{i+1}$; the B values, B_{ij}, are ordered so that $B_{ij} < B_{i,j+1}$. The B values are not necessarily the same on each L shell, i.e., $B_{ij} \neq B_{i+1,j}$. To obtain the flux at any point B', L', a four-point interpolation on the logarithm of the flux is performed.

The flux at the point (B', L'), where

$$L_i \leq L' \leq L_{i+1},$$

$$B_{ij} \leq B' \leq B_{i,j+1},$$

and

$$B_{i+1,k} \leq B' \leq B_{i+1,k+1}$$

is obtained by

$$F(B', L') = \exp \ell(B', L') .$$

Here

$$\ell(B', L') = \ell(B', L_i) + \left[\frac{\ell(B', L_{i+1}) - \ell(B', L_i)}{L_{i+1} - L_i}\right](L' - L_i) ,$$

$$\ell(B', L_i) = \ell(B_{ij}, L_i) + \left[\frac{\ell(B_{i,j+1}, L_i) - \ell(B_{ij}, L_i)}{B_{i,j+1} - B_{ij}}\right](B' - B_{ij}) ,$$

and

$$\ell(B', L_{i+1}) = \ell(B_{i+1,k}, L_{i+1})$$

$$+ \left[\frac{\ell(B_{i+1,k+1}, L_{i+1}) - \ell(B_{i+1,k}, L_{i+1})}{B_{i+1,k+1} - B_{i+1,k}}\right](B' - B_{i+1,k}) .$$

We have used a standard set of circular orbits between 150 and 6000 n mi altitude to do the orbital integrations for the inner zone environments. For altitudes below 4000 n mi, a time interval of one minute was found to be adequate and a total time of one day will average out longitudinal asymmetries produced by the anomalies in the magnetic field. For the altitudes 4000 through 6000 n mi, a two-minute step size and $T = 2$ days were used. These 76 orbits which comprise the standard set have been retained on punched cards so that calculations of B and L will not have to be repeated when integrations are done with new environments. For the low altitude orbits there are geographic regions where the flux is known to be negligible; a geographic test is made to determine if the flux should be set equal to zero without calculating B, L. This procedure reduces computer time considerably for low altitude orbits and has been used independently by others (Reference 9). An exclusion test for large L values is also used to reduce computer time when high inclination orbits are calculated. This is done by calculating L for a simple dipole and requiring that L be less than some desired value to continue the calculation at that point.

ELECTRON ENVIRONMENT AE1

The first model environment produced in this program was the inner zone electron model designated AE1. This was based on data available to us by June 1964. The main measurements that were used in constructing AE1 are shown in Table 1. We shall use the code shown in the last column in referring to the data hereafter. Since it was desired to present an environment as up-to-date as possible, data taken during late 1962 that presented evidence of injected electrons from the Russian detonations and their subsequent decay into the natural background have not been used.

At the time this environment was made, only the efficiency curve for E4 was available. The decay of the Starfish electrons during the time period of the various data also made it difficult to obtain good spectral information from the various threshold detectors. The model spectrum was obtained mainly from the detailed spectral measurements of E5 and E7. E7 covered the 1.17 to 1.70 L region, whereas E5 covered both the inner and outer zones in late 1962. At $L \approx 1.25$ and 1.7, the two measurements E5 and E7 were in good agreement. Above 2.0 MeV at all L values, an exponential spectrum gave a reasonable fit. The fact that E5 did not show a very large B dependence for the energy spectrum and the different energy threshold detectors exhibited similar shapes

Table 1

Data Used in Making AE1 Environment.

Laboratory	Satellite	Data Time Period	Type of Measurement	Nominal Energy Range (MeV)	Reference	Source of Data	Text Code For Data
University of California at San Diego	Explorer 15 1962 BΛ1	Oct. - Jan. 1962 - 63	J - Threshold Scintillator	> 0.5 > 5.0	McIlwain Reference 10	Flux Program obtained from McIlwain	E1 E2
	Relay 1 1962 BT1	May - Sept. 1963	$j_\perp$ - Threshold Scintillator	> 0.45	McIlwain et al. Reference 5	Reference	E3
Bell Telephone Laboratories	Relay 1 1962 BT1	Jan. - June 1963	$j_\perp$ - Threshold Scintillator	> 1.0	Brown et al. Reference 6	Reference	E4
Lawrence Radiation Laboratory	STARAD 1962 B-K	Oct. - Dec. 1962	j_1 - Beta Ray Spectrometer	0.325 - 3.25 in 5 channels	West et al. Reference 11	Reference	E5
Lockheed Missile and Space Company	1962 AT1	Sept. 1962	J - Threshold Scintillator	> 1.2	Imhof et al. Reference 12	Table obtained from Imhof	E6
	1963 - 42	Oct. - Nov. 1963	J - Scintillator PHA Spectrometer	0.3 - 13 MeV in 32 channels	Imhof et al. Reference 12, 13	Graphs obtained from Imhof	E7
State University of Iowa	Injun 3 1962 BT2	Dec. - Feb. 1962 - 63 June - July 1963	Shielded Geiger Tube	Brems-strahlung	Van Allen Reference 14	Reference	E8 E9
Aerospace Corporation	1962 BE1 1962 BO1	Oct. - Nov. 1962	Shielded Scintillation Counter	Brems-strahlung	Mihalov et al. Reference 15	Reference	E10

along a given L shell resulted in our using a model spectrum that depended only on L. An independent examination of E5 yielded similar results (Reference 9). In the region $1.25 < L < 1.7$ and $E < 2$ MeV, E5 and E7 were not in agreement. The reason for the differences are not clear but may be due to the energy dependence of Starfish decay (Reference 16), natural electron changes, or a large B dependence in the region where E7 was obtained. A compromise between the two measurements was used below $L = 1.7$, and E5 was followed closely at the higher L values although the effects of the Russian injections may have been present.

In order to examine the behavior of the high energy portion of the spectrum, we plotted the exponential parameter E_0 for some of the electron data (Figure 5). Since various curves could be drawn through the E5 data, we have presented the E_0 obtained from the curves given in Reference 11 as well as our own. The 0.5 MeV (E1) and >5.0 MeV (E2) measurements were used to obtain an E_0 although this was not expected to agree quantitatively with the other values because the spectrum is not exponential over the whole energy range. One sees the high energy portion of the spectrum gets soft as L increases from 1.2 to 1.8 and then becomes hard in the slot region $L = 2$ to 3. Although it is not completely clear that this behavior in the slot continued through the summer of 1963, other Relay I measurements of Brown et al. (Reference 6) indicated no spectral change out to $L = 2.3$ in this time period. The solid line in Figure 5 shows the L variation of E_0 that was chosen; the increase of E_0 above the 0.5 MeV minimum was delayed until $L = 1.9$ to obtain better agreement between E3 and E4. The differential spectrum obtained from these considerations is shown in Figures 6 through 9 and is given in Table 2 along with the integral spectrum.

Using this spectrum, all the data have been converted to >0.5 MeV so that a distribution function could be obtained. We show the results of this conversion in Figures 10 through 23 in the following manner. The individual measurements are shown as points at specific B values and the solid line represents the environment chosen. We show these at many L values because this is the best way to display the agreement of the data and to show those regions where no data existed. The E3 data were used initially with no energy correction but they have been plotted here using the efficiency curve shown in Figure 3. The $\bar{\epsilon}$ for both detectors using the model spectrum is given in Table 3 for a 0.5 MeV threshold energy. For E4, 1.0 and 1.7 MeV are also shown. It is seen that the higher energy detector shows larger changes to the L dependent spectrum the lower the threshold energy. All the other threshold data were converted to >0.5 MeV on the basis of the energies given in Table 1. The E5 data were not converted to omnidirectional flux, but it is shown where the two data overlap as the E1 data reduced by a factor of two are given in Reference 11. For L values above 2.5 only E1 and E2 were available, and E1 was used as being representative of the fluxes in this region although there are time changes that occur.

An examination of all these plots shows that the data spread over a considerable range and it is not really possible to see a systematic decay. Clearly the threshold for E2 depends on the spectrum as West, et al. (Reference 11) have pointed out. The agreement of E3 and E4 is reasonable up to $L = 1.9$; however to bring them in agreement at larger L values would require a considerably softer spectrum. The fact that the Brown, et al. detectors showed no spectral change in this time period makes this region a little uncertain. More recent data suggest considerable change in the high energy portion of the spectrum in this region.

Table 2

Energy Spectrum - AE1.

	L = 1.2		L = 1.3		L = 1.4		L = 1.5		L = 1.6		L = 1.7		L = 1.8	
E	N(E, .5)	N(>E, .5)	N(E, .5)	N(>E, .5)	N(E, .5)	N(>E, .5)	N(E, .5)	N(>E, .5)	N(E, .5)	N(>E, .5)	N(E, .5)	N(>E, .5)	N(E, .5)	N(>E, .5)
0.3	0.426	1.085	0.809	1.149	1.13	1.20	1.43	1.247	6.00	1.81	13.4	2.46	25.6	3.46
0.4	0.426	1.04	0.739	1.07	0.987	1.09	1.23	1.115	3.89	1.32	7.19	1.509	11.3	1.76
0.5	0.426	1.00	0.667	1.00	0.880	1.00	1.07	1.00	2.51	1.00	3.84	1.00	5.34	1.00
0.6	0.426	0.956	0.604	0.937	0.791	0.916	0.940	0.900	1.62	0.796	2.18	0.712	2.62	0.632
0.7	0.426	0.915	0.558	0.879	0.716	0.841	0.842	0.810	1.03	0.665	1.31	0.547	1.39	0.439
0.8	0.426	0.872	0.522	0.825	0.655	0.773	0.762	0.730	0.724	0.579	0.894	0.441	0.791	0.333
0.9	0.426	0.830	0.492	0.774	0.603	0.709	0.689	0.657	0.586	0.516	0.661	0.364	0.482	0.272
1.0	0.426	0.790	0.477	0.726	0.569	0.651	0.633	0.591	0.506	0.462	0.544	0.304	0.342	0.232
1.1	0.426	0.747	0.459	0.679	0.534	0.596	0.582	0.530	0.466	0.413	0.447	0.254	0.271	0.202
1.2	0.426	0.704	0.453	0.634	0.508	0.544	0.537	0.474	0.426	0.368	0.367	0.213	0.234	0.176
1.3	0.426	0.661	0.453	0.588	0.482	0.495	0.500	0.422	0.398	0.327	0.312	0.179	0.212	0.154
1.4	0.424	0.618	0.453	0.543	0.453	0.448	0.463	0.374	0.362	0.289	0.266	0.151	0.194	0.134
1.5	0.411	0.575	0.447	0.498	0.427	0.405	0.432	0.329	0.338	0.254	0.226	0.126	0.178	0.115
1.6	0.396	0.533	0.429	0.454	0.404	0.363	0.401	0.288	0.315	0.221	0.192	0.1048	0.161	9.82-2
1.7	0.372	0.492	0.404	0.412	0.378	0.324	0.378	0.248	0.298	0.190	0.162	8.70-2	0.144	8.28-2
1.8	0.357	0.455	0.371	0.373	0.349	0.287	0.359	0.212	0.278	0.162	0.137	7.20-2	0.127	6.90-2
1.9	0.332	0.422	0.338	0.337	0.320	0.253	0.325	0.178	0.251	0.135	0.115	5.94-2	0.110	5.71-2
2.0	0.305	0.390	0.302	0.305	0.289	0.222	0.282	0.147	0.222	0.111	9.72-2	4.86-2	9.36-2	4.70-2
3.0	0.138	0.178	0.113	0.113	7.94-2	6.00-2	4.18-2	2.16-2	3.00-2	1.52-2	1.31-2	6.52-3	1.26-2	6.28-3
3.5	9.30-2	0.121	6.88-2	6.91-2	4.13-2	3.14-2	1.58-2	8.23-3	1.11-2	5.55-3	4.86-3	2.46-3	4.68-3	2.34-3
4.0	6.07-2	8.18-2	4.26-2	4.16-2	2.18-2	1.64-2	6.16-3	3.16-3	4.06-3	2.02-3	1.78-3	8.90-4	1.71-3	8.50-4
5.0	2.71-2	3.77-2	1.58-2	1.55-2	6.12-3	4.53-3	9.04-4	4.61-4	5.60-4	2.77-4	2.45-4	1.22-4	2.36-4	1.16-4
6.0	1.19-2	1.70-2	5.98-3	5.79-3	1.73-3	1.23-3	1.36-4	6.78-5	7.66-5	3.65-5	3.35-4	1.68-5	3.23-5	1.59-5
7.0	5.27-3	7.78-3	2.25-3	2.12-3	4.96-4	3.35-4	2.05-5	6.60-6	1.05-5	4.90-6	4.62-6	2.32-6	4.45-6	2.18-6

Table 2 (Continued)

Energy Spectrum - AE1.

E	L = 1.9		L = 2.0		L = 2.1		L = 2.2		L = 2.3 - 2.7		L = 2.8 - 3.0	
	N(E, .5)	N(>E, .5)	N(E, .5)	N(>E, .5)	N(E, .5)	N(>E, .5)	N(E, .5)	N(>E, .5)	N(E, .5)	N(>E, .5)	N(E, .5)	N(>E, .5)
0.3	27.3	3.54	16.8	2.76	10.7	2.24	7.76	1.87	1.70	1.19	2.43	1.27
0.4	11.9	1.79	8.40	1.59	5.79	1.45	4.14	1.31	0.907	1.07	1.25	1.09
0.5	5.59	1.00	4.27	1.00	3.25	1.00	2.33	1.00	0.496	1.00	0.641	1.00
0.6	2.70	0.616	2.31	0.685	1.81	0.757	1.29	0.826	0.279	0.963	0.348	0.953
0.7	1.42	0.421	1.30	0.507	1.00	0.619	0.719	0.728	0.158	0.943	0.198	0.928
0.8	0.800	0.313	0.749	0.408	0.627	0.535	0.417	0.672	0.103	0.930	0.127	0.914
0.9	0.475	0.252	0.462	0.349	0.406	0.486	0.256	0.641	8.81-2	0.920	0.113	0.900
1.0	0.305	0.214	0.336	0.309	0.308	0.450	0.193	0.618	9.07-2	0.912	0.130	0.890
1.1	0.209	0.190	0.277	0.279	0.259	0.423	0.181	0.602	0.109	0.902	0.188	0.874
1.2	0.176	0.171	0.231	0.253	0.236	0.399	0.191	0.582	0.139	0.889	0.261	0.850
1.3	0.170	0.154	0.218	0.230	0.234	0.375	0.208	0.562	0.183	0.874	0.328	0.821
1.4	0.170	0.137	0.202	0.209	0.234	0.352	0.231	0.540	0.288	0.852	0.382	0.785
1.5	0.168	0.120	0.190	0.190	0.234	0.329	0.265	0.516	0.336	0.824	0.415	0.745
1.6	0.160	0.103	0.183	0.171	0.234	0.305	0.288	0.489	0.427	0.785	0.435	0.704
1.7	0.148	8.75-2	0.175	0.153	0.234	0.282	0.305	0.458	0.478	0.739	0.439	0.658
1.8	0.132	7.34-2	0.165	0.136	0.234	0.258	0.308	0.428	0.482	0.692	0.431	0.615
1.9	0.118	6.08-2	0.153	0.120	0.228	0.235	0.299	0.398	0.474	0.643	0.415	0.575
2.0	0.100	5.00-2	0.140	0.105	0.213	0.213	0.288	0.368	0.443	0.598	0.395	0.534
3.0	1.35-2	6.85-3	3.64-2	2.78-2	7.74-2	7.70-2	0.129	0.168	0.205	0.276	0.189	0.254
3.5	5.00-3	2.50-3	1.88-2	1.41-2	4.72-2	4.68-2	8.63-2	0.114	0.141	0.188	0.130	0.174
4.0	1.83-3	9.35-4	9.52-3	7.35-3	2.83-2	2.86-2	6.01-2	7.75-2	9.56-2	0.128	9.21-2	0.122
5.0	2.52-4	1.24-4	2.52-3	1.91-3	1.06-2	1.05-2	2.73-2	3.54-2	4.40-2	5.97-2	4.43-2	5.93-2
6.0	3.45-5	1.74-5	6.79-4	4.99-4	3.96-3	3.90-3	1.27-2	1.63-2	2.04-2	2.74-2	2.14-2	2.81-2
7.0	4.75-6	2.42-6	1.81-4	1.32-4	1.48-3	1.45-3	5.92-3	7.45-3	9.52-3	1.28-2	1.03-2	1.36-2

Table 3

Average Efficiency for E3 and E4 Detectors.

L	Detector E3		Detector E4	
	$\bar{\epsilon}_{0.5}$	$\bar{\epsilon}_{0.5}$	$\bar{\epsilon}_{1.0}$	$\bar{\epsilon}_{1.7}$
1.2	0.93	6.28×10^{-2}	7.95×10^{-2}	12.8×10^{-2}
1.3	1.00	5.39×10^{-2}	7.41×10^{-2}	13.1×10^{-2}
1.4	1.01	4.35×10^{-2}	6.68×10^{-2}	13.4×10^{-2}
1.5	1.01	3.51×10^{-2}	5.94×10^{-2}	14.1×10^{-2}
1.6	1.09	2.72×10^{-2}	5.89×10^{-2}	14.3×10^{-2}
1.7	1.23	1.50×10^{-2}	4.93×10^{-2}	17.2×10^{-2}
1.8	1.44	1.28×10^{-2}	5.52×10^{-2}	15.4×10^{-2}
1.9	1.45	1.27×10^{-2}	5.92×10^{-2}	14.5×10^{-2}
2.0	1.29	2.56×10^{-2}	8.29×10^{-2}	16.7×10^{-2}
2.1	1.21	4.13×10^{-2}	9.18×10^{-2}	14.6×10^{-2}
2.2	1.16	5.50×10^{-2}	8.90×10^{-2}	12.0×10^{-2}
2.3 - 2.7	1.03	8.65×10^{-2}	9.46×10^{-2}	11.7×10^{-2}
2.7 - 3.0	1.07			

We tended to normalize the environment near E3 because this was a later time measurement and fell in the middle of much of the converted data. At higher L values the model falls closer to E1. At low altitudes electrons are wiped off in the South Atlantic anomaly as they drift eastward and the depleted regions are repopulated during the remainder of the drift around the earth (References 13, 17, and 18). This produces a longitudinal variation that becomes pronounced for mirror points whose minimum altitudes lie deep in the atmosphere. The low altitude fluxes also vary with magnetic activity based on more recent data (Reference 18). In this first electron environment we have not attempted to represent these effects in detail and have bounded the map at low altitudes by making the lowest flux contour (10^3) follow the line $h_{min} = 0$ km over much of the B-L space. Clearly there are both time and longitudinal variations in this region.

The final F-B curves were obtained by comparing with the B-L flux map representation and making adjustments consistent with the data until smooth curves were produced in both representations. The final results are shown in Figures 24 through 26 as F-B, B-L and R-λ flux maps. The numerical values are available on punched cards and have been distributed to many organizations.

The orbital integrations were performed with this environment by the method described in Section VII. The spectrum was handled in the following way. At each L value

$$L_i = 1.1 + 0.1i$$

up to L = 3.0, the fraction of the particles in each of eight energy bands as given in Table 4 was specified. The computer used this as the spectrum over the whole interval

$$L_i - 0.05 \le L < L_i + 0.05 \ .$$

The final results are given in Figure 27 for E > 0.5 MeV. The results for all the energy bands have been distributed in tabular form. The equatorial pitch angle distribution or $j_\perp$ obtained by the conversion program described in Section III is shown in Figure 28.

Table 4

Fraction of Electrons in Energy Bands (MeV) - Map AE1.

E(I)	E(I+1)	L < 1.25	1.25 ≤ L < 1.35	1.35 ≤ L < 1.45	1.45 ≤ L < 1.55	1.55 ≤ L < 1.65
0.50	1.00	0.2100E-00	0.2740E-00	0.3490E-00	0.4090E-00	0.5380E-00
1.00	2.00	0.4000E-00	0.4210E-00	0.4290E-00	0.4440E-00	0.3510E-00
2.00	3.00	0.2120E-00	0.1920E-00	0.1620E-00	0.1250E-00	0.9580E-01
3.00	4.00	0.9620E-01	0.7140E-01	0.4360E-01	0.1880E-01	0.1320E-01
4.00	5.00	0.4410E-01	0.2610E-01	0.1190E-01	0.2740E-02	0.1720E-02
5.00	6.00	0.2070E-01	0.9700E-02	0.3270E-02	0.3920E-03	0.2440E-03
6.00	7.00	0.9200E-02	0.3700E-02	0.8950E-03	0.6140E-04	0.3110E-04
7.00	∞	0.7800E-02	0.2100E-02	0.3350E-03	0.6600E-05	0.4900E-05

E(I)	E(I+1)	1.65 ≤ L < 1.75	1.75 ≤ L < 1.85	1.85 ≤ L < 1.95	1.95 ≤ L < 2.05	2.05 ≤ L < 2.15
0.50	1.00	0.6960E-00	0.7680E-00	0.7860E-00	0.6910E-00	0.5500E-00
1.00	2.00	0.2550E-00	0.1850E-00	0.1640E-00	0.2040E-00	0.2370E-00
2.00	3.00	0.4240E-01	0.4070E-01	0.4320E-01	0.7720E-01	0.1360E-00
3.00	4.00	0.5710E-02	0.5450E-02	0.5870E-02	0.2050E-01	0.4840E-01
4.00	5.00	0.7680E-03	0.7340E-03	0.8060E-03	0.5390E-02	0.1810E-01
5.00	6.00	0.1050E-03	0.1000E-03	0.1070E-03	0.1410E-02	0.6600E-02
6.00	7.00	0.1470E-04	0.1380E-04	0.1460E-04	0.3680E-03	0.2450E-02
7.00	∞	0.2300E-05	0.2200E-05	0.2400E-05	0.1320E-03	0.1450E-02

E(I)	E(I+1)	2.15 ≤ L < 2.25	2.25 ≤ L < 2.75	2.75 ≤ L < 3.05
0.50	1.00	0.3820E-00	0.8800E-01	0.1100E-00
1.00	2.00	0.2500E-00	0.3140E-00	0.3560E-00
2.00	3.00	0.2000E-00	0.3220E-00	0.2800E-00
3.00	4.00	0.9050E-01	0.1480E-00	0.1320E-00
4.00	5.00	0.4210E-01	0.6830E-01	0.6270E-01
5.00	6.00	0.1910E-01	0.3230E-01	0.3120E-01
6.00	7.00	0.8850E-02	0.1460E-01	0.1450E-01
7.00	∞	0.7450E-02	0.1280E-01	0.1360E-01

UPDATING OF THE ELECTRON ENVIRONMENT

An updating of the inner zone electron environment will be undertaken in the near future as soon as additional information is available. There will be spectral data from the EGO and P-11 satellites as well as extensive mapping from Relay II, Injun IV, and Explorer 26 in the near future.

Some recent work by Walt (Reference 19) and Walt and McDonald (Reference 20) has shown that atmospheric scattering and energy loss explain the decay of the Starfish residue very well for L < 1.25, but theory and observation depart radically at higher L values. Experimental decay lifetimes for ~2 MeV electrons have been reported by Van Allen (Reference 21) and for >1.2 MeV by Bostrom and Williams (Reference 16). We show these results in Figure 29. Hess (Reference 22) has used the lifetimes quoted in Reference 16 to decay his E8 grid from November 1962 to January 1965, and has cautioned correctly that no account has been taken of the energy dependence of the decay nor is one certain when the other energies will reach the natural background.

We have used the AE1 spectrum to convert the Bostrom and Williams >1.2 MeV measurements at L = 1.2, 1.3, 1.4, 1.5, 1.6, 1.7 to >0.5 MeV using the efficiency curve given in Reference 23. Examples of these results are given in Figures 13 and 14. With these results and the measured lifetimes we have calculated the time between their later measurements and AE1; the resulting time intervals are given in Table 5. It is seen that the ratio of their data and AE1 vary with L. The average interval over all L's would place the time of AE1 around 1 March 1963. Based on the normalization of AE1 near the E3 measurement, we would expect the date of AE1 to be 1 July 1963 and recommend using this date for decay purposes. The spread between the AP1 data and AE1 after correction for decay is about the same as much of the data in Table 1. Using the Bostrom and Williams decay values, we have performed orbital integrations for AE1 decayed in July 1, 1965. The results are given in Figure 32 along with the original results from AE1 for comparison.

Table 5

Decay Interval: AE1 Map and Bostrom-Williams Data Days 64-70, 1964.

L	Time Interval (Days)
1.2	262
1.3	347
1.4	402
1.5	418
1.6	414
Avg.	369

THE INNER ZONE PROTON ENVIRONMENT

The inner zone proton flux is relatively stable in time although some changes at low altitudes occur over the solar cycle because of atmospheric changes. The magnitude of this effect seems to be less than that predicted by Blanchard and Hess (Reference 24) probably because of errors in the atmospheric model chosen. McIlwain (Reference 25) has observed a radical decrease in the high energy component >34 MeV for L > 2.0 following the large magnetic storm of 23 September 1963 and is observing the slow return of this to prestorm values (Reference 26). Farther out in the magnetosphere, the proton distributions are more easily affected by magnetic disturbances but in general they are more stable than the electron fluxes.

Although emulsions have been used to make some spectral measurements at low altitudes, most of the information concerning the distribution and energy spectrum has been obtained from threshold detectors which usually measure within an energy window. The model environments described in this section will be for energies above 4 MeV. The lower energy protons which extend throughout the outer zone will be treated at a later date. The satellite data that have been used in constructing the proton maps are given in Tables 6 and 7. We shall refer to the data by the code name given in these tables.

For certain energy intervals and for large regions of space the integral spectrum can be represented by an exponential spectrum. To illustrate this point we show the Naugle and Kniffen data (Reference 27) at high B values in Figure 33 and the equatorial spectrum obtained on Relay I (Reference 28) in Figure 34. These both suggest that the sum of two exponentials would be good over much of the inner zone. We have attempted to represent the environment in this fashion but have found this is too restrictive to describe the whole spatial and energy domain we desire to include. Instead, we have broken up the environment into four energy bands: 4 to 15, 15 to 30, 30 to 50, and >50 MeV and have used an exponential spectrum within each band. The energy parameter, E_0, is a function of both B and L so we are representing the omnidirectional integral flux as

$$J(>E, B, L) = F(B, L)\, e^{E_1 - E/E_0(B, L)} .$$

By selecting a known energy function, we can still represent the environment in terms of functions of two variables rather than the more cumbersome general function of three variables.

Proton Map AP1

We will discuss the various environments in the same sequence in which they were derived. The data above 30 MeV were studied first. We have used the published energy intervals or thresholds for each srt of data. There were not many efficiency curves available and even if there were, the effort was not considered necessary in this first attempt at describing the environment. We did use the energy interval 50 to 75 MeV for the Telstar data although it has been referred to as >50 MeV in some cases. This choice was based on the published detector efficiency in a typical direction (Reference 33) and this choice gave better agreement with other data in all regions except where the spectrum was very hard.

The function E_0 (B, L) obtained for this region is given in Figure 35 and we show the data converted to flux >34 MeV in Figures 36 through 52. This conversion is described in Section IV. We have selected E_1 = 34 MeV because the P6 data are the most extensive at the higher L values where there are not enough data to obtain a good spectrum.

At low L and high B values the 1958 to 1961 data (P1, P2, and P3) seem to be separated from the 1962 data (P4) and probably reflect the solar cycle changes that are predicted. An examination of Figures 37 through 42 shows the effect diminishing as L increases or, more appropriately, as h_{min} increases. We have made the model conform with the later data because of the time period assigned to the environment. The divergence of the Telstar data at high B values where the spectrum is hard is probably due to an energy dependence of energy window values. Of course this is probably true of the other detectors also. At any rate, we have selected the lines shown in the figures as

Table 6

Data Used in Making AP1, AP2 and AP3 Environments.

Laboratory	Satellite	Data Time Period	Type of Measurement	Nominal Energy Range (MeV)	Reference	Source of Data	Text Code for Data
State University of Iowa	Explorer 4 1958 E 1	July - Oct. 1958	J, Geiger Tube	> 31 > 43	McIlwain Reference 29	Reference	P1
Applied Physics Laboratory	Injun 1 1961 02	July - Dec. 1961	J, Geiger Tube	> 40	Bostrom, et al. Reference 30	Reference	P3
Aerospace Corporation	1962 AT1 1962 BE1	Sept. - Oct. 1962	J, Solid State	60 - 120	Freden and Paulikas Reference 31	Reference	P4
University of California at San Diego	Explorer 15 1962 BΛ1	Oct. - Jan. 1962 - 63	J, Scintillator	40-110	McIlwain Reference 10	Flux Program	P5
	Relay 1 1962 BT1	May - Sept. 1963	J, Scintillator $j_\perp$, Scintillator	> 34 18.2 - 35	McIlwain, et al. Reference 5	Reference	P6 P7
	Injun 3 1962 BT2	Dec. - Sept. 1962 - 63	J, Scintillator	40-110	Valerio Reference 32	Reference	P8
Bell Telephone Laboratories	Telstar 1 1962 AE1	July - Feb. 1962 - 63	J, Solid State	50 - 75	Brown, et al. Reference 33	Analytical fit obtained from Brown and Gabbe	P9
Lockheed Missile and Space Company	1962 K1	April 1962	J, Scintillator	> 59	Imhof and Smith Reference 34	Reference	P10

Table 7

Data Used in Making AP4 Environment.

Laboratory	Satellite	Data Time Period	Type of Measurement	Nominal Energy Range (MeV)	Reference	Source of Data	Text Code for Data
Aerospace Corporation	1962 AT1 1962 BE1	Sept. - Oct. 1962	J, Solid State	5 - 20	Freden and Paulikas Reference 31	Reference	P11
Bell Telephone Laboratories	Relay 1 1962 BT1	Dec. - Jan. 1962 - 63	$j_\perp$, Solid State	5 - 8.6	Brown, et al. Reference 6	Reference	P12
	Explorer 15 1962 BΛ1	Oct. - Jan. 1962 - 63	J, Solid State	4-13	Private Communication	Analytical fit and plots obtained from Brown and Gabbe	P13
University of California at San Diego	Relay 1 1962 BT1	May - Sept. 1963	$j_\perp$, Solid State	> 5.2	McIlwain, et al. Reference 5	Reference	P14

being representative. The resulting distribution function is shown in the three representations commonly used to display environments in Figures 53 through 55.

Proton Map AP2

From the examination of Figures 33 and 34, one suspects that the spectral slope will change radically somewhere in the region between 6 and 20 MeV depending on the B, L coordinates. Since there were very little data in this energy interval, we decided to make the change at 15 MeV independent of the spatial point.

The AP2 environment was constructed by using P7 data and the AP1 distribution function to obtain the E_0 function to be used in the 15 to 30 MeV interval. This function is shown in Figure 56, and comparison with Figure 37 shows that the two are very similar. In fact, it is possible to use AP2 over a wider energy range than 15 to 30 MeV without much error. The various forms of the distribution function are given in Figures 57 through 59.

Proton Map AP3

It is interesting to note that the spectrum gets softer on a given L shell as one approaches the equator, at least for $L < 2.0$ over the energy range 15 to 50 MeV. At the higher energies the opposite effect occurs on the basis of the data of Imhof and Smith (Reference 34) and the recent measurements of Freden, Blake, and Paulikas (Reference 35). Therefore, an additional map had to be constructed to describe the high energy protons.

There were very little data available above 60 MeV with which to obtain an environment. However using the data of References 34 and 35 along with that of Garmire (Reference 36) we have obtained E_0 for the high energy map which we have designated AP3. The distribution function for AP3 is produced by AP1 for $E > 50$ MeV and the various representations are shown in Figures 60 through 62. The E_0 is plotted in Figure 63.

Proton Map AP4

Although there are data available down to 1 MeV in the inner zone, the spectrum changes enough that a map AP4 only covering the 4 to 15 MeV energy range was made. Extensions to lower energy will be done in the near future. The data used in making AP4 are given in Table 7. An estimate of the proper spectrum around 4 MeV in the inner zone was made using the P12 - P14 data as well as the 1.1 to 14 MeV protons measured by McIlwain, et al. (Reference 5) and the 2.5 to 3.8 MeV protons measured by Brown, et al. (Reference 6). The differential spectrum near the equator is shown in Figure 63. It is clear than an exponential integral spectrum in this region is not completely correct, but it is adequate for our purposes as long as one considers $E > 4$ MeV. The comparison of this model with the data is shown in Figures 65 through 79. The discrepancies at the low L values are believed to be partly due to our choice of the spectrum. It is obvious from the figures that we have followed P13 closely; this was the only measurement available above

$L_* = 3.0$ in the energy range. The three representations of the distribution function are shown in Figures 80 through 82 and the spectral parameter is plotted in Figure 83. The equatorial omnidirectional fluxes calculated with the proton environment are given in Figure 84 for various energies. The perpendicular fluxes, $j_\perp$, for the four maps obtained by the conversion program discussed in Section III are shown in Figures 85 through 88.

Using these omnidirectional flux maps, the orbital integrations for the standard circular orbits were performed. The logarithmic interpolation described in Section VII was used for both $F(B, L)$ and $E_0(B, L)$. Although the four maps AP1 to 4 are most accurate over the energy bands described earlier, it is possible to obtain reasonable answers outside these bands. Since it is sometimes cumbersome to use more than one map for a specific purpose, we have computed the orbital integrations for 23 energy intervals with each map. These intervals are given in Table 8; it is hoped that these results will be useful in selecting a map best suited for a given purpose. The results of these calculations are too extensive to be included here but will be available under separate cover. We provide an example of the printout in Table 9. We show some of the orbital integration results for each map in Figures 89 through 92.

Table 8

Energy Bands Used in Orbital Integrations.

AP1		AP2		AP3		AP4	
5 - 10		5 - 10		5 - 10		1 - 2	
10 - 15		10 - 15		10 - 15		2 - 3	
15 - 20		15 - 20	Recommended	15 - 20		3 - 4	
20 - 25		20 - 25	Range	20 - 25		4 - 5	
25 - 30		25 - 30		25 - 30		5 - 6	
30 - 35		30 - 35		30 - 35		6 - 7	
35 - 40	Recommended	35 - 40		35 - 40		7 - 8	
40 - 45	Range	40 - 45		40 - 45		8 - 9	
45 - 50		45 - 50		45 - 50		9 - 10	Recommended
50 - 60		50 - 60		50 - 60		10 - 11	Range
60 - 70		60 - 70		60 - 70		11 - 12	
70 - 80		70 - 80		70 - 80		12 - 13	
80 - 90		80 - 90		80 - 90		13 - 14	
90 - 100		90 - 100		90 - 100		14 - 15	
100 - 110		100 - 110		100 - 110		15 - 20	
110 - 120		110 - 120		110 - 120	Recommended	20 - 25	
120 - 130		120 - 130		120 - 130	Range	25 - 30	
130 - 140		130 - 140		130 - 140		30 - 35	
140 - 150		140 - 150		140 - 150		35 - 40	
150 - 200		150 - 200		150 - 200		40 - 45	
200 - 250		200 - 250		200 - 250		45 - 50	
250 - 300		250 - 300		250 - 300		50 - 60	
300 - ∞		300 - ∞		300 - ∞		60 - 70	

Table 9

Example of Orbital Integrations Printout

Orbital Integration Map AP1.

Orbit Altitude: 150 n mi   Total Time: 24 Hours   Time Interval: 1 Minute

Orbit Inclination Degrees		0		30		60		90	
E_k	E_{k+1}	$\Phi(>E_k)$	$\Phi(E_{k+1} - E_k)$	$\Phi(>E_k)$	$\Phi(E_{k+1} - E_k)$	$\Phi(>E_k)$	$\Phi(E_{k+1} - E_k)$	$\Phi(>E_k)$	$\Phi(E_{k+1} - E_k)$
5	10	0.	0.	0.400E 06	0.845E 04	0.272E 07	0.170E 07	0.287E 07	0.199E 07
10	15	0.	0.	0.392E 06	0.825E 04	0.101E 07	0.479E 06	0.879E 06	0.471E 06
15	20	0.	0.	0.384E 06	0.807E 04	0.534E 06	0.147E 06	0.407E 06	0.120E 06
20	25	0.	0.	0.376E 06	0.788E 04	0.386E 06	0.519E 05	0.287E 06	0.360E 05
25	30	0.	0.	0.368E 06	0.771E 04	0.334E 06	0.225E 05	0.251E 06	0.145E 05
30	35	0.	0.	0.360E 06	0.753E 04	0.312E 06	0.127E 05	0.237E 06	0.848E 04
35	40	0.	0.	0.352E 06	0.736E 04	0.299E 06	0.927E 04	0.228E 06	0.650E 04
40	45	0.	0.	0.345E 06	0.720E 04	0.290E 06	0.784E 04	0.222E 06	0.571E 04
45	50	0.	0.	0.338E 06	0.703E 04	0.282E 06	0.715E 04	0.216E 06	0.530E 04
50	60	0.	0.	0.331E 06	0.136E 05	0.275E 06	0.132E 05	0.211E 06	0.991E 04
60	70	0.	0.	0.317E 06	0.130E 05	0.262E 06	0.123E 05	0.201E 06	0.928E 04
70	80	0.	0.	0.304E 06	0.124E 05	0.249E 06	0.115E 05	0.191E 06	0.876E 04
80	90	0.	0.	0.292E 06	0.118E 05	0.238E 06	0.109E 05	0.183E 06	0.830E 04
90	100	0.	0.	0.280E 06	0.113E 05	0.227E 06	0.104E 05	0.174E 06	0.788E 04
100	110	0.	0.	0.269E 06	0.108E 05	0.216E 06	0.989E 04	0.167E 06	0.748E 04
110	120	0.	0.	0.258E 06	0.103E 05	0.206E 06	0.940E 04	0.159E 06	0.710E 04
120	130	0.	0.	0.247E 06	0.993E 04	0.197E 06	0.893E 04	0.152E 06	0.675E 04
130	140	0.	0.	0.237E 06	0.949E 04	0.188E 06	0.849E 04	0.145E 06	0.642E 04
140	150	0.	0.	0.228E 06	0.908E 04	0.180E 06	0.808E 04	0.139E 06	0.610E 04
150	200	0.	0.	0.219E 06	0.398E 05	0.172E 06	0.349E 05	0.133E 06	0.263E 05
200	250	0.	0.	0.179E 06	0.320E 05	0.137E 06	0.273E 05	0.106E 06	0.206E 05
250	300	0.	0.	0.147E 06	0.258E 05	0.109E 06	0.215E 05	0.860E 05	0.163E 05
300	∞	0.	0.	0.121E 06	0.121E 06	0.882E 05	0.882E 05	0.697E 05	0.697E 05

REFERENCES

1. Vette, J. I., "The Updating and Dissemination of the Knowledge of Trapped Radiation - Model Environments:" Proceedings of the Second Symposium on Protection Against Radiation in Space, NASA SP-71, 47-55, 1965.

2. Roberts, C. S., "On the Relationship Between the Unidirectional and Omnidirectional Flux of Trapped Particles on a Magnetic Line of Force," *J. Geophys. Res.* 70:2517-2528, 1965.

3. Ray, E. C., "On the Theory of Protons Trapped in the Earth's Magnetic Field," *J. Geophys. Res.* 65:1125-1134, 1960.

4. Farley, T. A., and Sanders, N. L., "Pitch Angle Distributions and Mirror Point Densities in the Outer Radiation Zone," *J. Geophys. Res.* 67:2159-2168, 1962.

5. McIlwain, C. E., Fillius, R. W., Valerio, J., and Dave, A., "Relay I Trapped Radiation Measurements," NASA TND 2516, 1964.

6. Brown, W. L., Davidson, L. W., and Medford, L. V., "The Energetic Particle Environment of Relay I: Bell Telephone Laboratories Experiments."

7. "Useful High-Altitude Nuclear Effects Computer Programs Volume 2 Geomagnetic Codes," RM 63TMP-28 NASA 1311-2, 1963.

8. Jensen, D. C., and Cain, J. C., "An Interim Geomagnetic Field," *J. Geophys. Res.* 67:3568-3569, 1962 Abstract.

9. "Computer Codes for Space Radiation Environment and Shielding, Volume I," TDR WL TDR-64-71, Air Force Weapons Laboratory, 1964.

10. McIlwain, C. E., "The Radiation Belts, Natural and Artificial," *Science* 142:355-361, 1963.

11. West, Jr., H. I., Mann, L. G., and Bloom, S. D., "Some Electron Spectra in the Radiation Belts in the Fall of 1962," in: *Space Research V Proc. 5th Internat. Space Sci. Sympos., Florence, May 12-16, 1964.* Ed. by D. G. King-Hele, P. Muller, G. Righini, Amsterdam: North-Holland Publishing Co. 1965, pp. 423-445.

12. Imhof, W. L., et al., "Analysis and Evaluation of Geomagnetically Trapped Electrons from High Altitude Nuclear Explosions," NASA Report No. 1540, July 1964.

13. Imhof, W. L., and Smith, R. V., "Longitudinal Variations of High Energy Electrons at Low Altitudes," *J. Geophys. Res.* 70:569-578, 1965.

14. Van Allen, J. A., "Further Observations on the Starfish and Soviet Artificial Radiation Belts," SUI-63-37, State University of Iowa, 1963.

15. Mihalov, J. D., Mozer, F. S., and White, R. S., "Artificially Injected Electrons at Low Altitude," *J. Geophys. Res.* 69:4003-4014, 1964.

16. Bostrom, C. O., and Williams, D. J., "Time Decay of the Artificial Radiation Belt," *J. Geophys. Res.* 70:240-242, 1965.

17. Paulikas, G. A., and Freden, S. C., "Precipitation of Energetic Electrons into the Atmosphere," *J. Geophys. Res.* 69:1239-1250, 1964.

18. Williams, D. J., and Kohl, J. W., "Loss and Replenishment of Electrons at Middle Latitudes and High B Values," *J. Geophys. Res.* 70:4139-4150, 1965.

19. Walt, M., "The Effects of Atmospheric Collisions on Geomagnetically Trapped Electrons, *J. Geophys. Res.* 69:3947-3958, 1962.

20. Walt, M., and MacDonald, W. M., "The Influence of the Earth's Atmosphere on Geomagnetically Trapped Particles," *Reviews of Geophysics* 2:543-578, 1964.

21. Van Allen, J. A., "Lifetimes of Geomagnetically Trapped Electrons of Several MeV Energy," *Nature* 203:1006-1007, 1964.

22. Hess, W. N., Letter to Users of the E8 Grid, Oct. 20, 1964.

23. Williams, D. J., and Smith, A. M., "Daytime Trapped Electron Intensities at High Latitudes at 1100 Kilometers," *J. Geophys. Res.* 70:541-556, 1965.

24. Blanchard, R. C., and Hess, W. N., "Solar Cycle Changes in Inner Zone Protons," *J. Geophys. Res.* 69:3927-3938, 1964.

25. McIlwain, C. E., "The Redistribution of Trapped Protons During a Magnetic Storm," in: *Space Research V Proc. 5th Internat. Space Sci. Sympos., Florence, May 12-16, 1964.* Ed. by D. G. King-Hele, P. Muller, G. Righini, Amsterdam: North-Holland Publishing Co. 1965, pp. 374-391.

26. McIlwain, C. E., "Long-Term Changes in the Distribution of the 40-110 MeV Trapped Protons," *Trans. Am. Geophys. Union* 46:141, 1965.

27. Naugle, J. E., and Kniffen, D. A., "Variations of the Proton Energy Spectrum with Position in the Inner Van Allen Belt," *J. Geophys. Res.* 68:4065-4078, 1963.

28. Fillius, R. W., and McIlwain, C. E., "The Anomalous Energy Spectrum of Protons in the Earth's Radiation Belt," *Phys. Rev. Letters* 12:609-612, 1964.

29. McIlwain, C. E., "Coordinates for Mapping the Distribution of Magnetically Trapped Particles," *J. Geophys. Res.* 66:3681-4078, 1963.

30. Bostrom, C. O., Zmuda, A. J., and Pieper, G. F., "Trapped Protons in the South Atlantic Magnetic Anomaly During July - December 1961, 2. Comparisons with NERV and Relay I and the Energy Spectrum," *J. Geophys. Res.* 70:2035-2044, 1965.

31. Freden, S. C., and Paulikas, G. A., "Trapped Protons at Low Altitudes in the South Atlantic Anomaly," *J. Geophys. Res.* 69:1259-1270, 1964.

32. Valerio, J., "Protons from 40 - 110 MeV Observed in Injun 3," *J. Geophys. Res.* 69:4949-4958, 1964.

33. Brown, Buck, Medford, Thomas, Gummel, Miller and Swits, "The Spacecraft Radiation Experiments," The Bell System Technical Journal, Vol. XLII, 899-941, 1963.

34. Imhof, W. L., and Smith, R. V., "Proton Intensities and Energy Spectrums in the Inner Van Allen Belt," *J. Geophys. Res.* 69:91-100, 1964.

35. Freden, S. C., Blake, J. B., and Paulikas, G. A., "Spatial Variation of the Trapped Proton Spectrum," *J. Geophys. Res.* 70:3111-3116, 1965.

36. Garmire, G., "Geomagnetically Trapped Protons with Energies Greater than 350 MeV," *J. Geophys. Res.* 68:2627-2638, 1963.

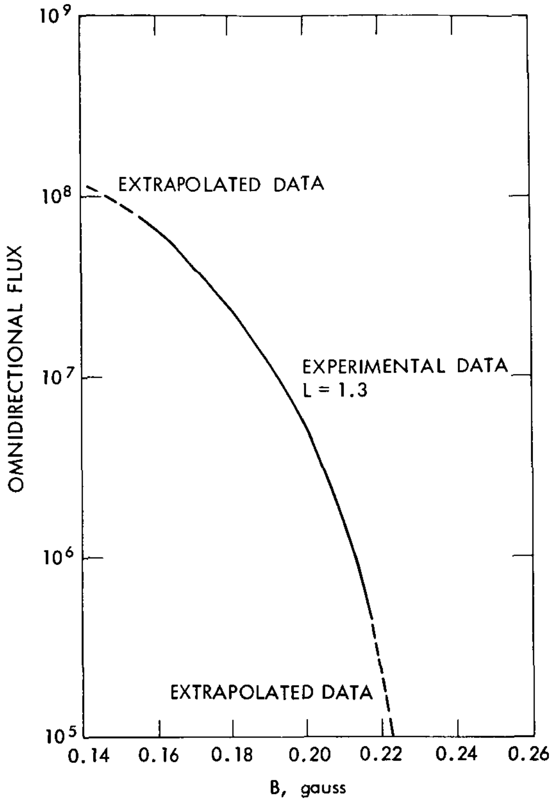

Figure 1—Illustration of real and extrapolated data used in the conversion program. By extending the data, on both sides if necessary, the conversion of the flux is more correct near the end points of the real data.

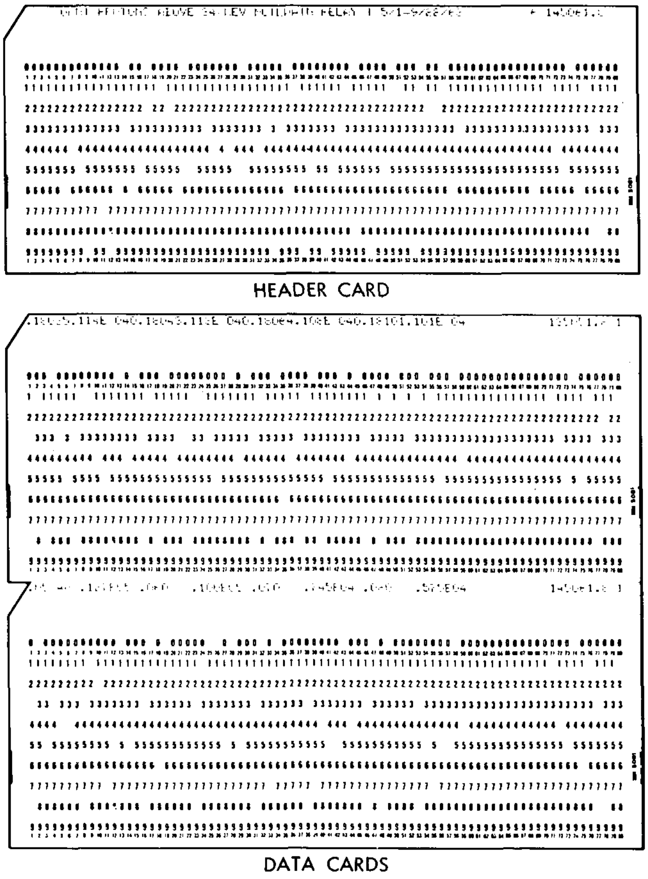

Figure 2—Examples of header and data cards used to store the trapped radiation data. The two data cards show different positions of the flux values within the field. See text for explanation.

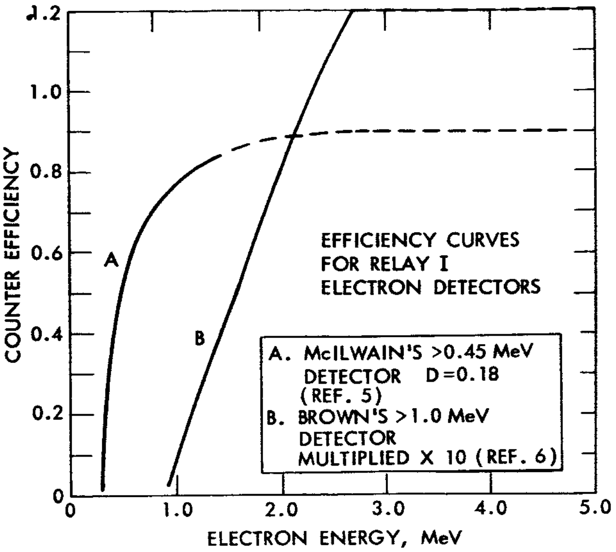

Figure 3—Counter efficiency versus energy for two detectors flown on the Relay I satellite.

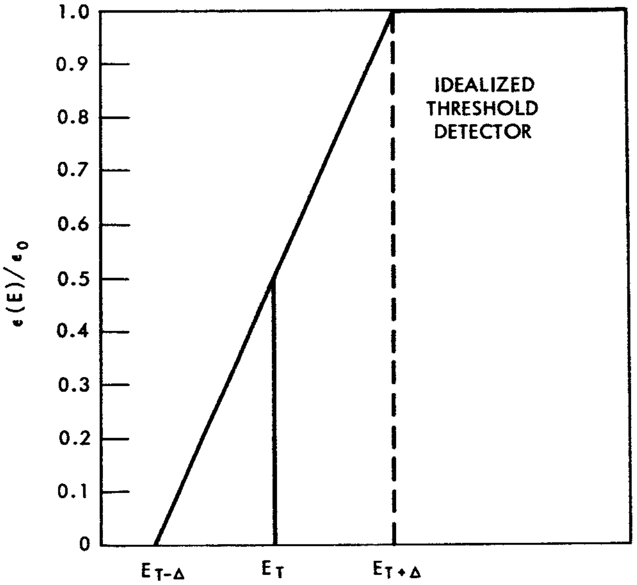

Figure 4—Idealized threshold detector efficiency curve versus energy. The quantity ϵ_0 is the maximum efficiency reached at any energy.

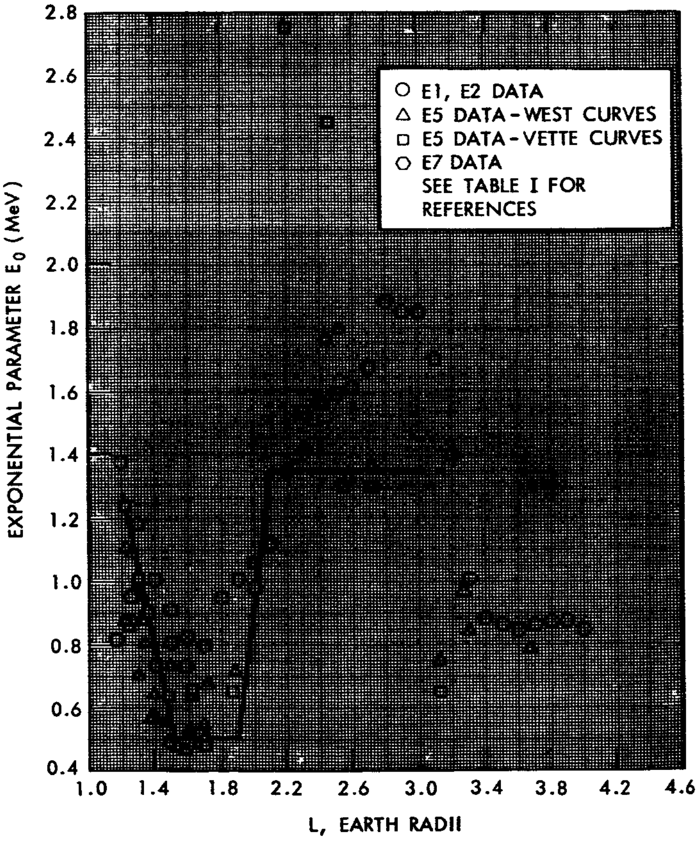

Figure 5—The exponential energy parameter versus L for electron data. The solid curve is the variation of E_0 chosen for the AE1 model environment. This model spectrum is exponential above 2.0 MeV.

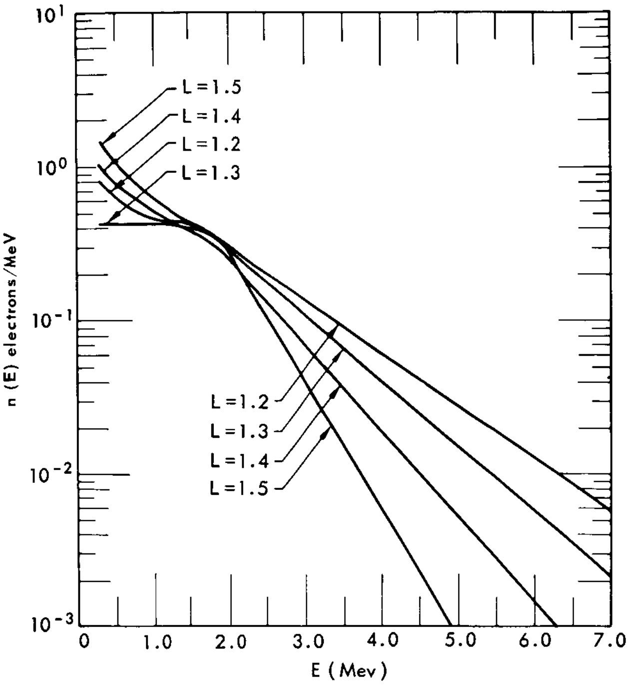

Figure 6—The differential spectra for AE1 at L = 1.2, 1.3, 1.4, and 1.5.

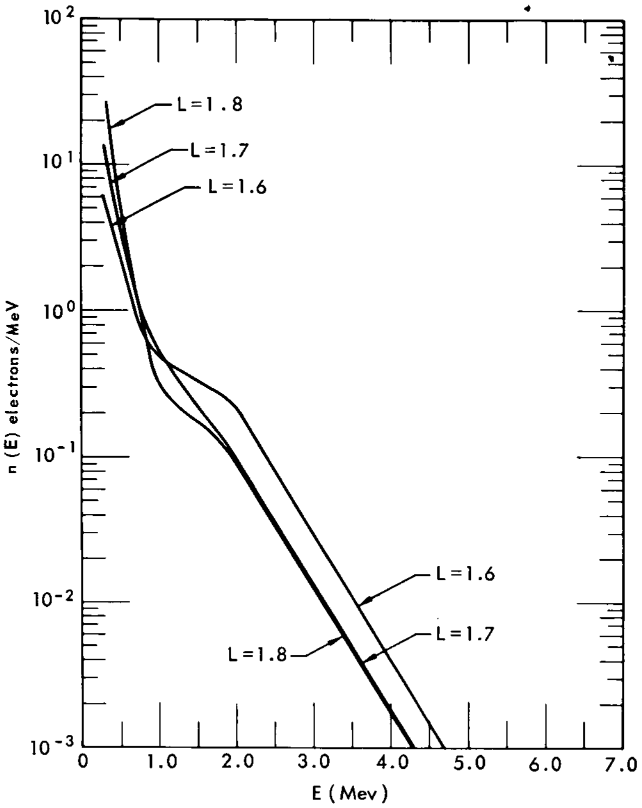

Figure 7—The differential spectra for AE1 at L = 1.6 1.7, and 1.8.

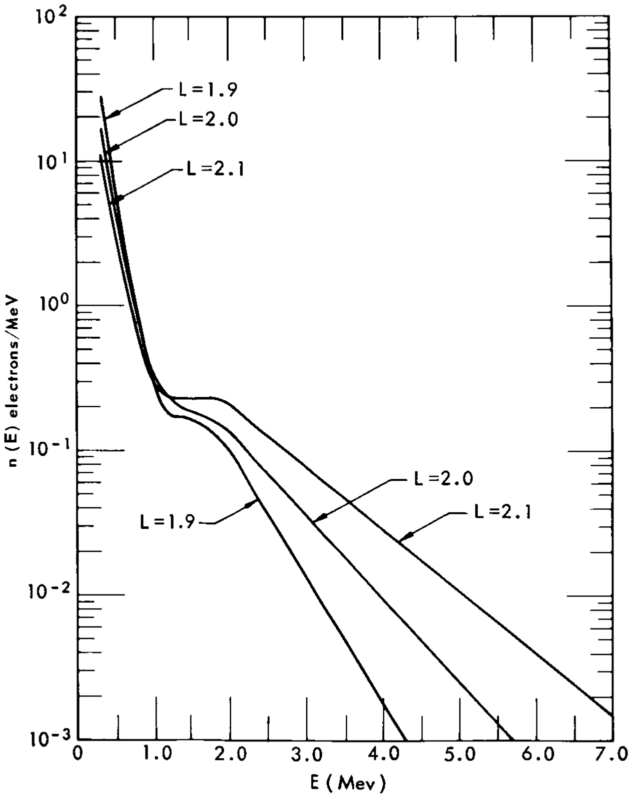

Figure 8—The differential spectra for AE1 at L = 1.9, 2.0, and 2.1.

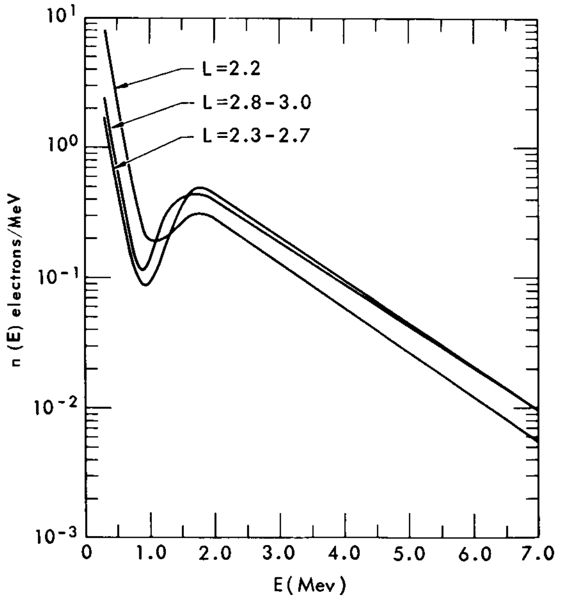

Figure 9—The differential energy spectra for AE1 at L = 2.2, 2.3 - 2.7, 2.8 - 3.0. An average spectrum is used over the L bands 2.3 - 2.7 and 2.8 - 3.0 because the change is small and the data limited.

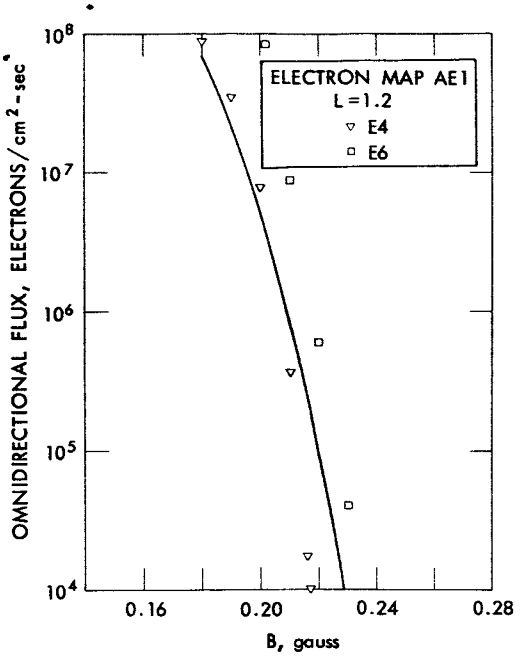

Figure 10—Comparison of electron map AE1 with experimental data at L = 1.2. The measured data are converted to the omnidirectional flux above 0.5 MeV by means of the model spectrum. The coded points are identified in Table 1.

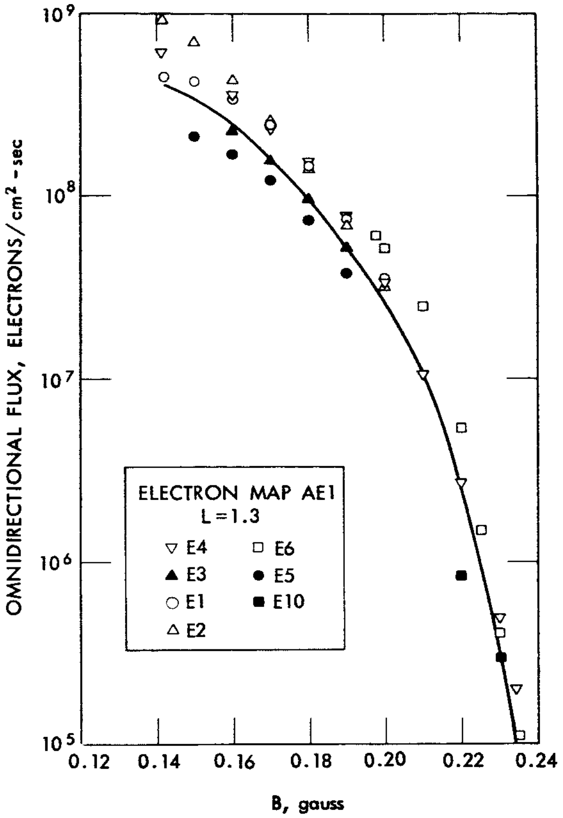

Figure 11—Comparison of electron map AE1 with experimental data at L = 1.3.

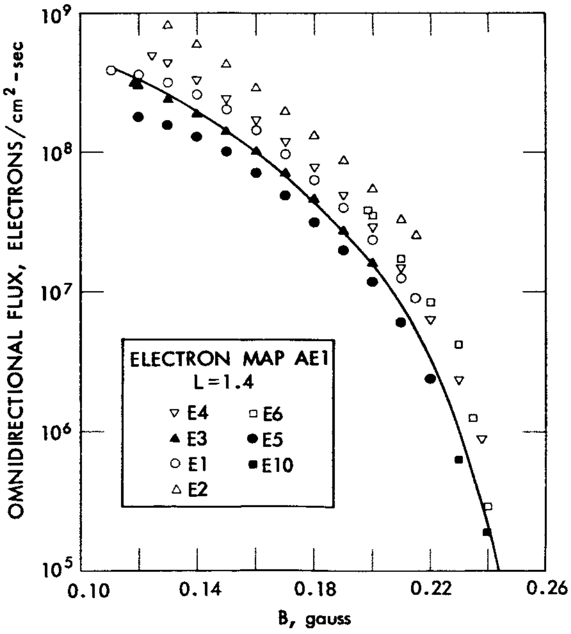

Figure 12—Comparison of electron map AE1 with experimental data at L = 1.4.

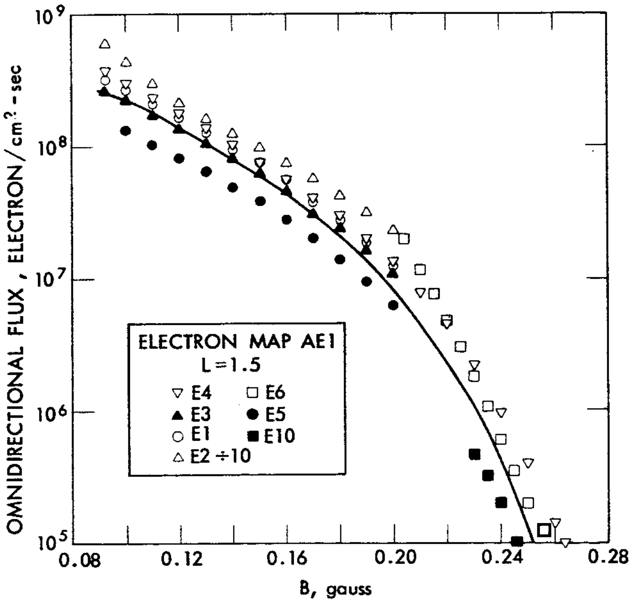

Figure 13—Comparison of electron map AE1 with experimental data at L = 1.5.

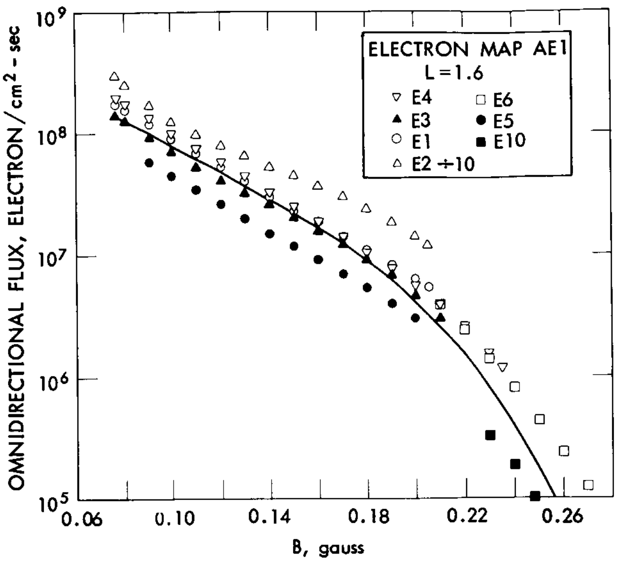

Figure 14—Comparison of electron map AE1 with experimental data at L = 1.6.

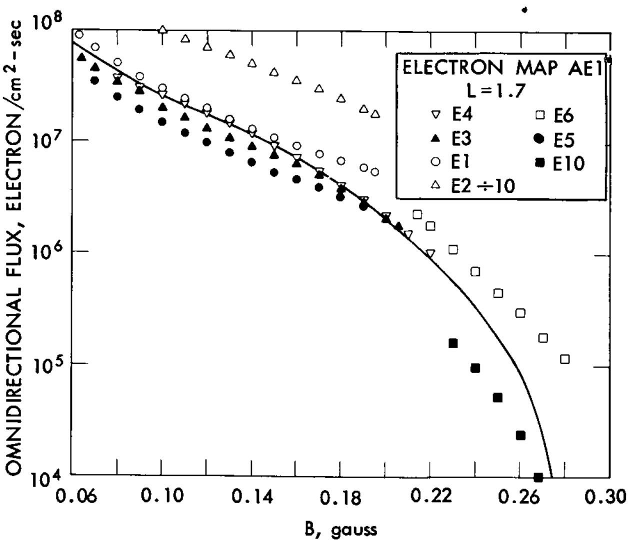

Figure 15—Comparison of electron map AE1 with experimental data at L = 1.7.

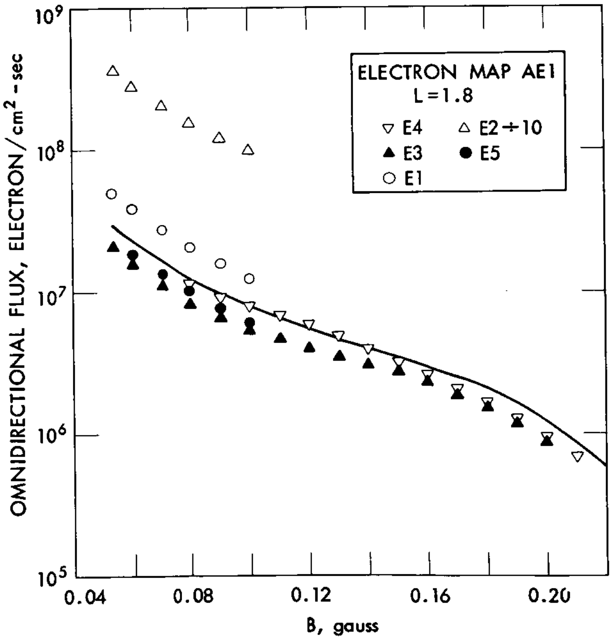

Figure 16—Comparison of electron map AE1 with experimental data at L = 1.8.

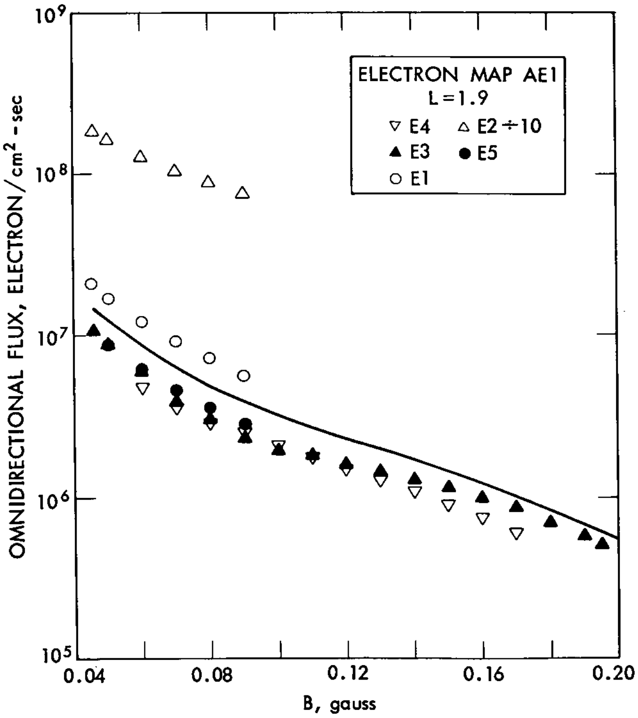

Figure 17—Comparison of electron map AE1 with experimental data at L = 1.9.

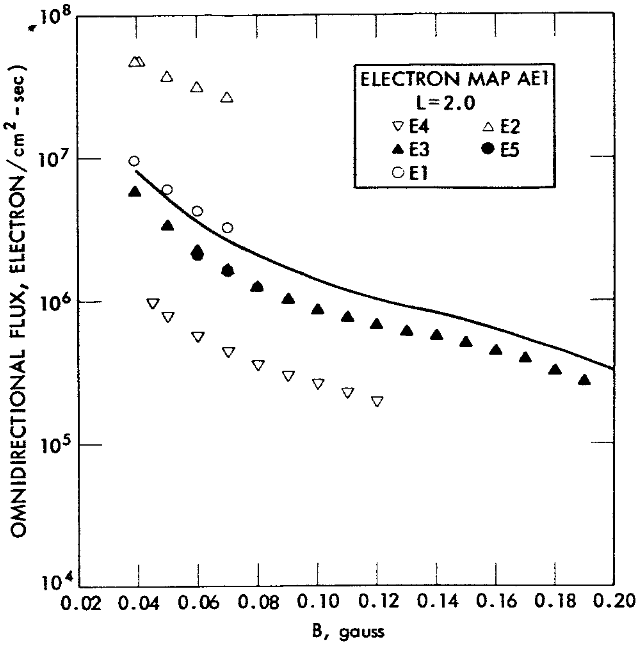

Figure 18—Comparison of electron map AE1 with experimental data at L = 2.0.

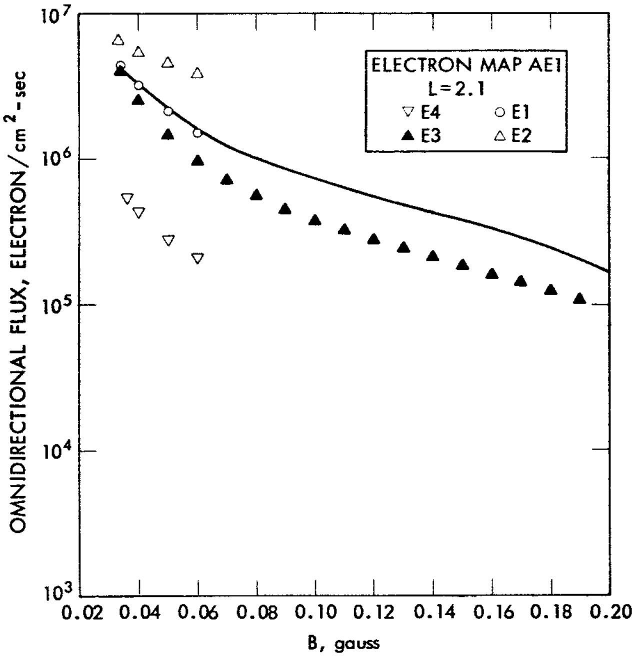

Figure 19—Comparison of electron map AE1 with experimental data at L = 2.1.

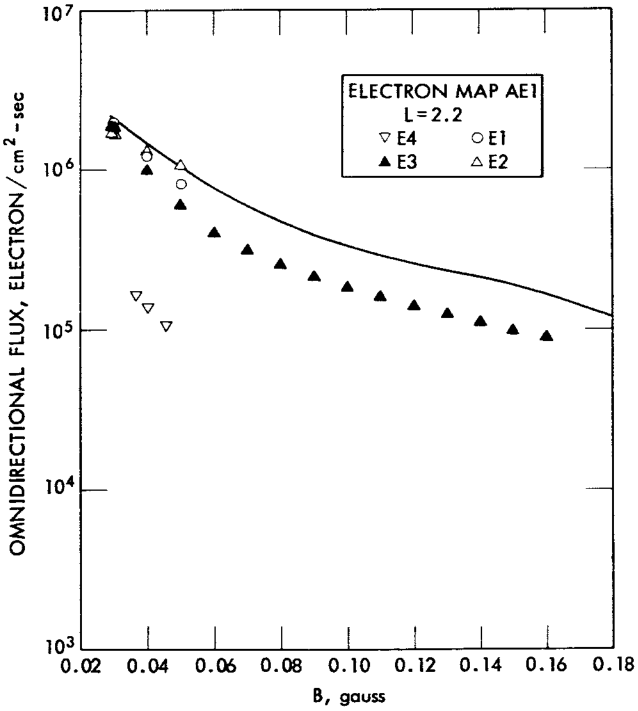

Figure 20—Comparison of electron map AE1 with experimental data at L = 2.2.

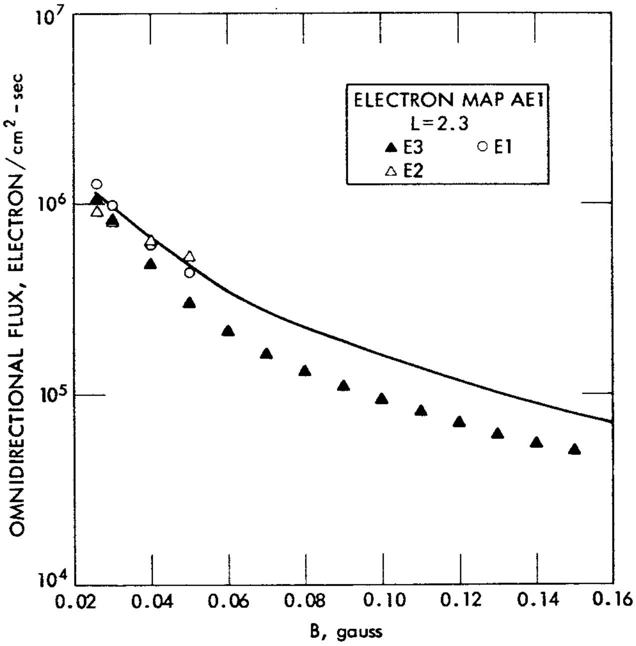

Figure 21—Comparison of electron map AE1 with experimental data at L = 2.3.

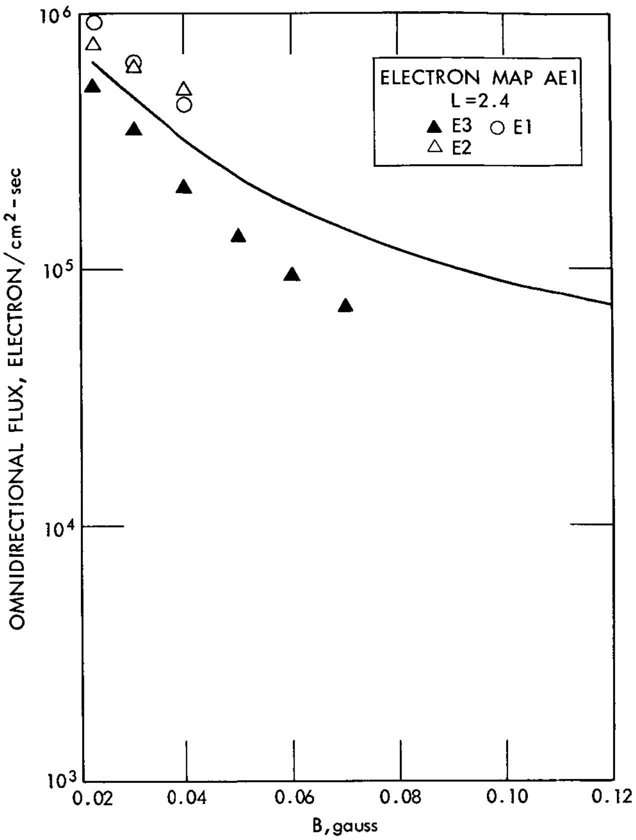

Figure 22—Comparison of electron map AE1 with experimental data at L = 2.4.

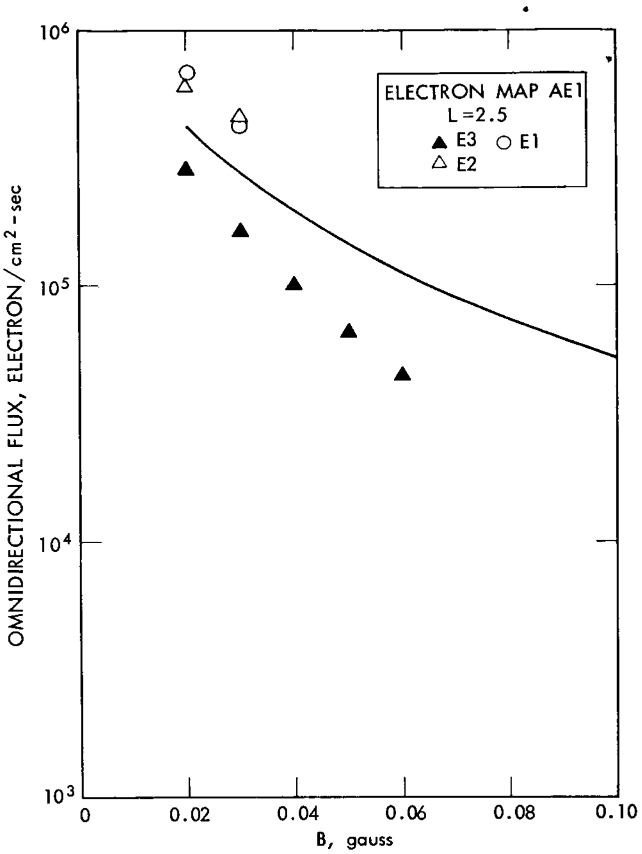

Figure 23—Comparison of electron map AE1 with experimental data at L = 2.5.

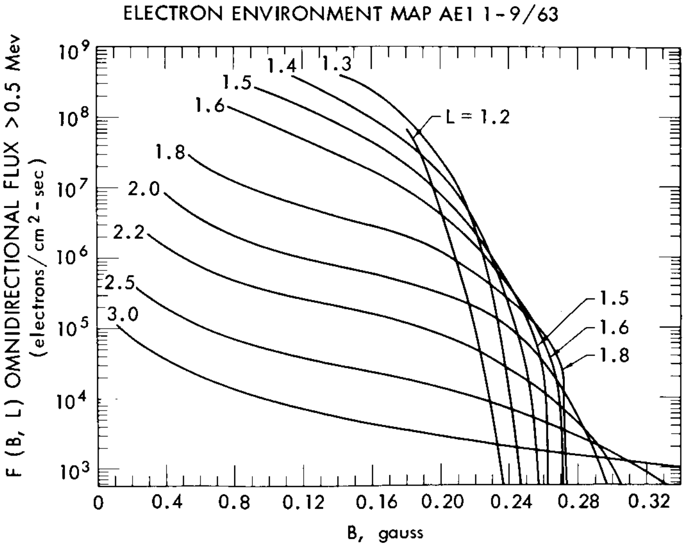

Figure 24—The flux versus B plot of AE1, E > 0.5 MeV.

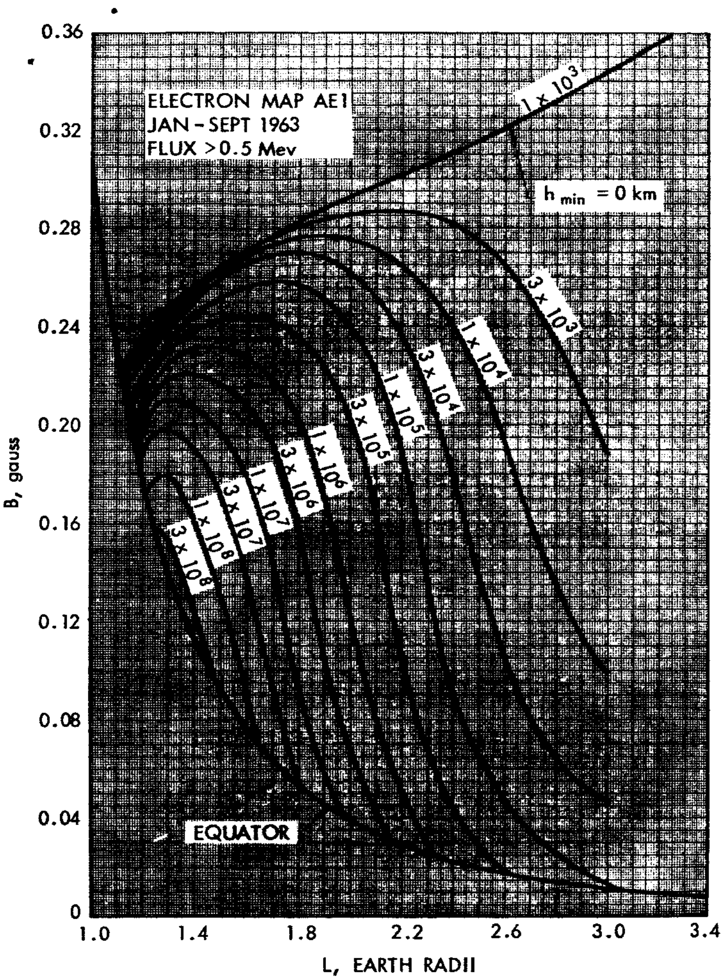

Figure 25—The B-L flux map for AE1, E > 0.5 MeV.

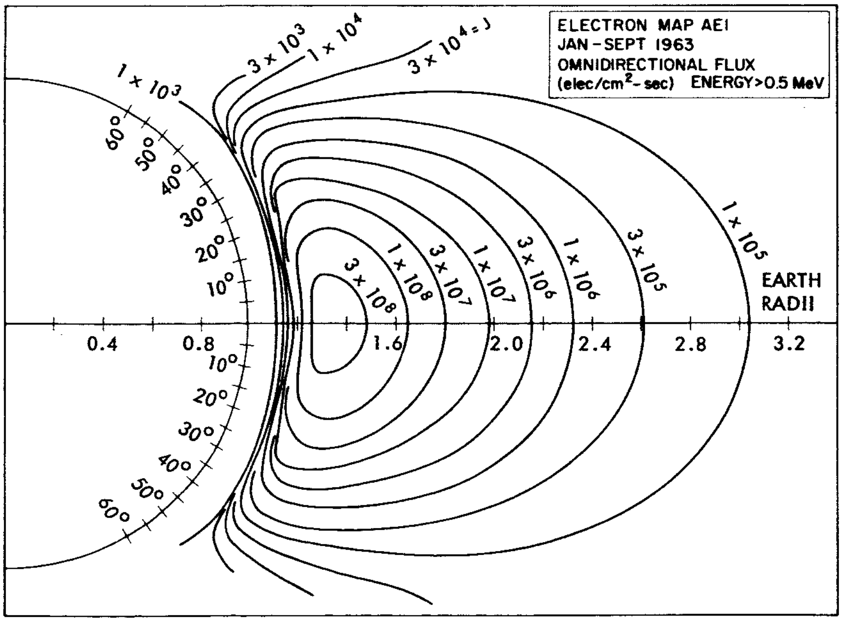

Figure 26—The R-λ flux map for AE1, E > 0.5 MeV.

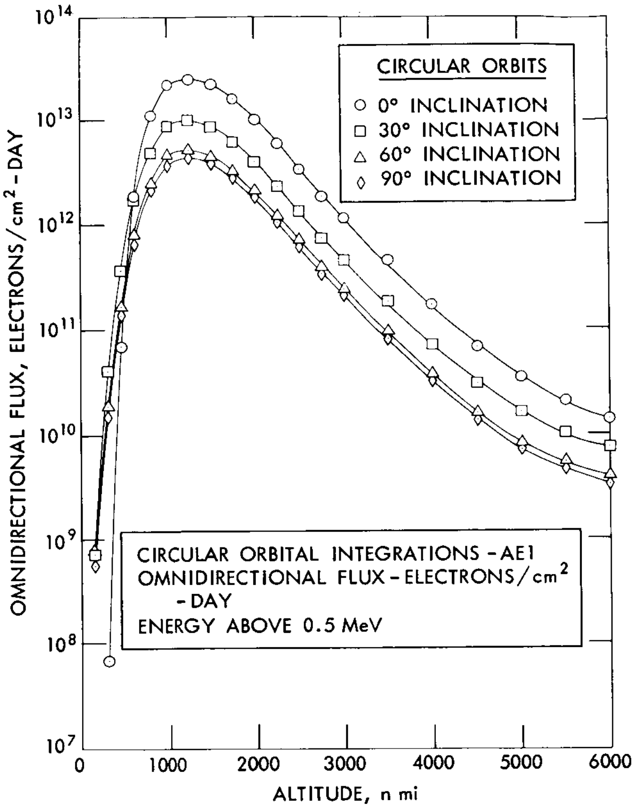

Figure 27—Orbital integrations with AE1, E > 0.5 MeV for circular orbits.

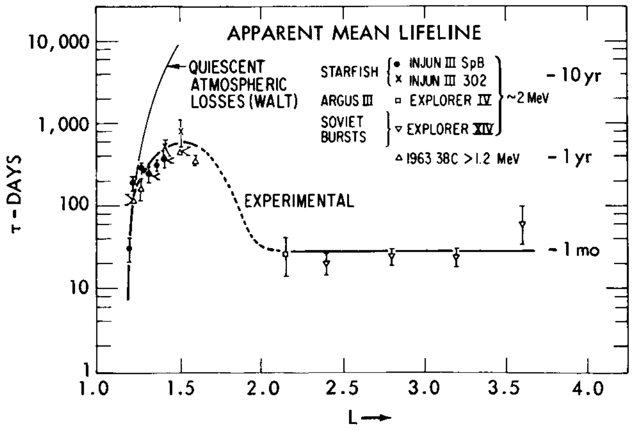

Figure 29—Apparent mean lifetimes of energetic electrons versus L. The results of several satellites are combined to show the general agreement of the measurements and to demonstrate the shorter lifetime for L > 2.0.

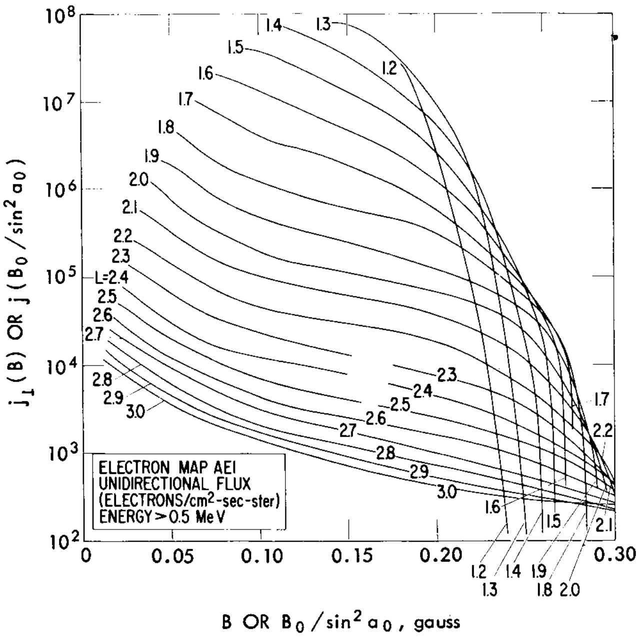

Figure 28—The flux versus B plot for $j_\perp$ or $j(B_o/\sin^2\alpha_o)$ of AE1.

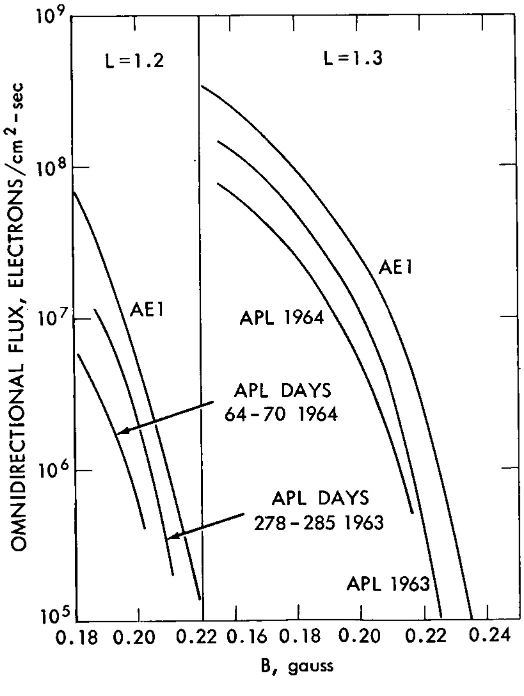

Figure 30—Comparison of AE1 and the APL measurements from satellite 1963 - 38c at L = 1.2 and 1.3. The data of Bostrom and Williams (Ref. 16) for Oct. 15-22, 1963 and March 4-10, 1964 are converted to > 0.5 MeV using the model spectrum of AE1.

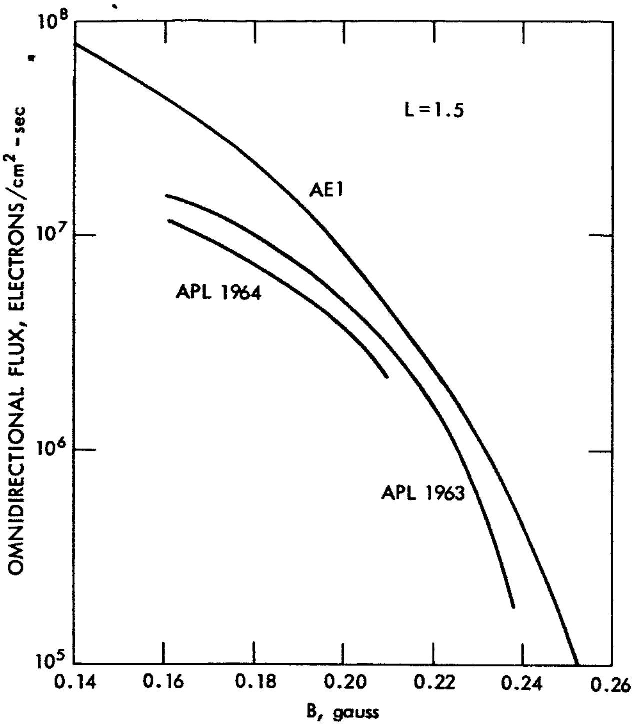

Figure 31—Comparison of AE1 and the AP1 measurements from satellite 1963 - 38c at L = 1.5. The shapes of the AP1 data and AE1 are less similar at this L value than those shown in Fig. 30.

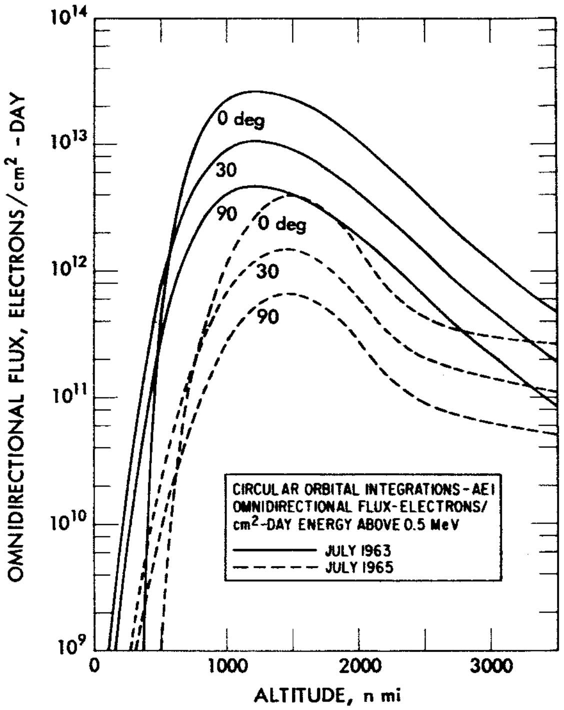

Figure 32—Comparison of orbital integrations with AE1 for July 1, 1963 and July 1, 1965. The 1965 results were obtained by using the Bostrom-Williams decay constants and a time period of two years from the original AE1 environment. The angles shown are the orbit inclination angles.

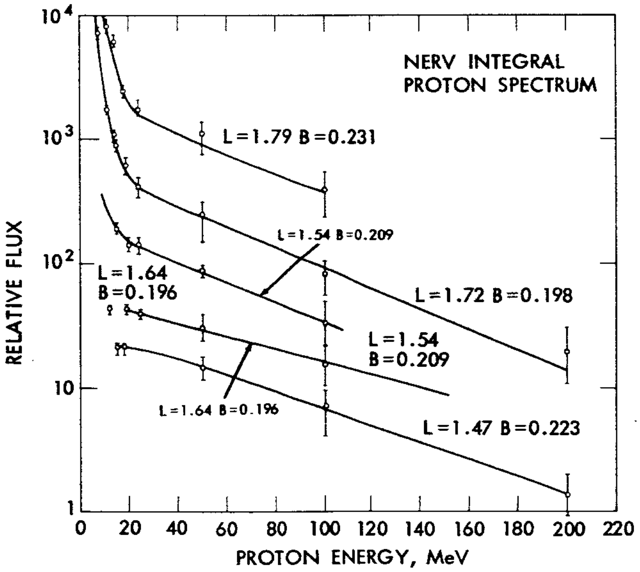

Figure 33—Integral proton spectra obtained with the NERV experiment. The solid lines through the points at L = 1.79, 1.72, and 1.64 are the sum of two exponential spectra.

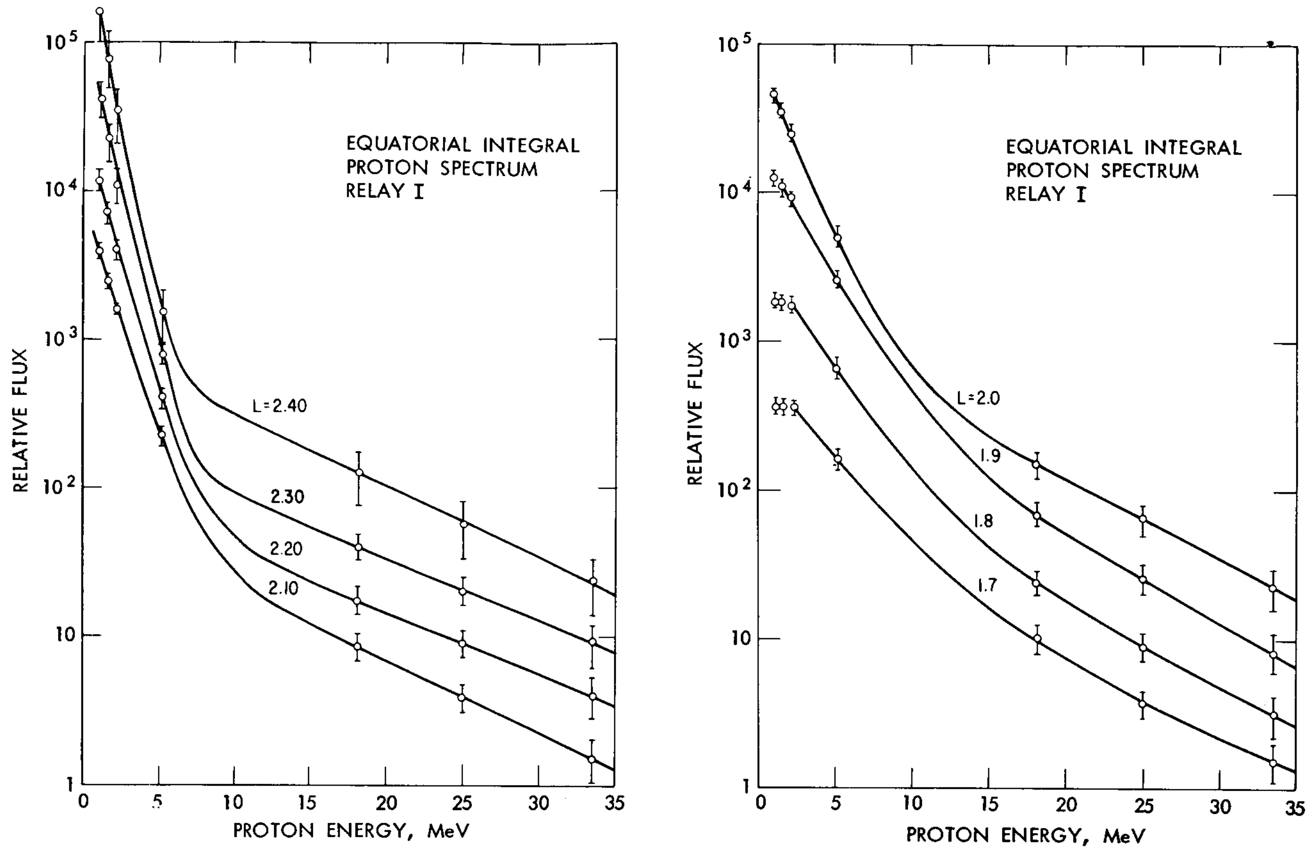

Figure 34—Integral proton spectra obtained at the equator with Relay I. The solid lines drawn through the points are the sum of two exponential spectra.

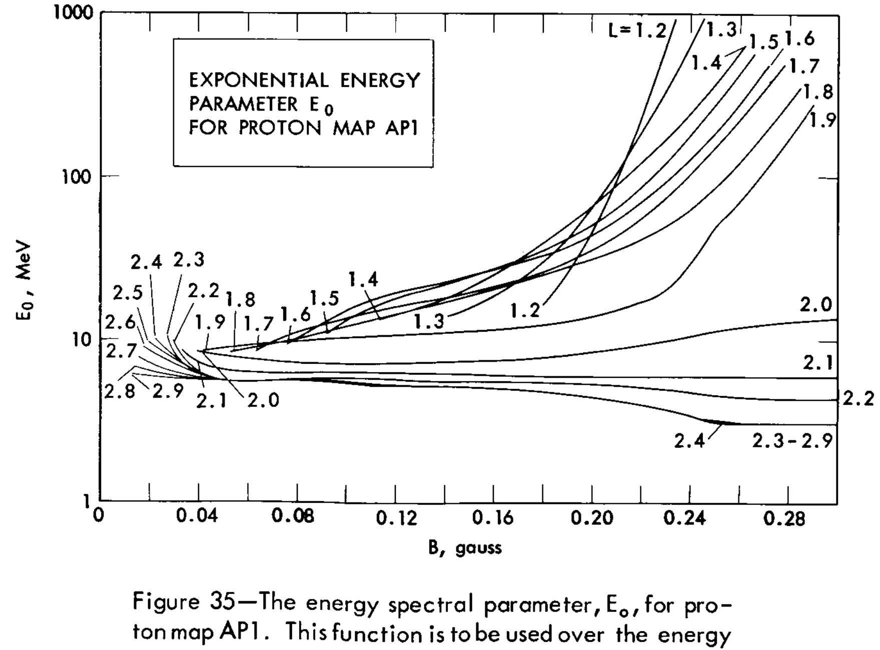

Figure 35—The energy spectral parameter, E_o, for proton map AP1. This function is to be used over the energy range 30 - 50 MeV.

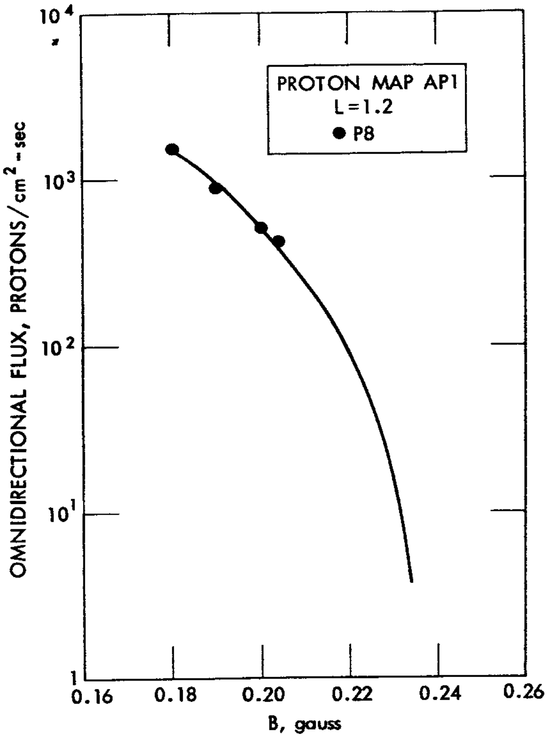

Figure 36—Comparison of proton map AP1 with experimental data at L = 1.2.

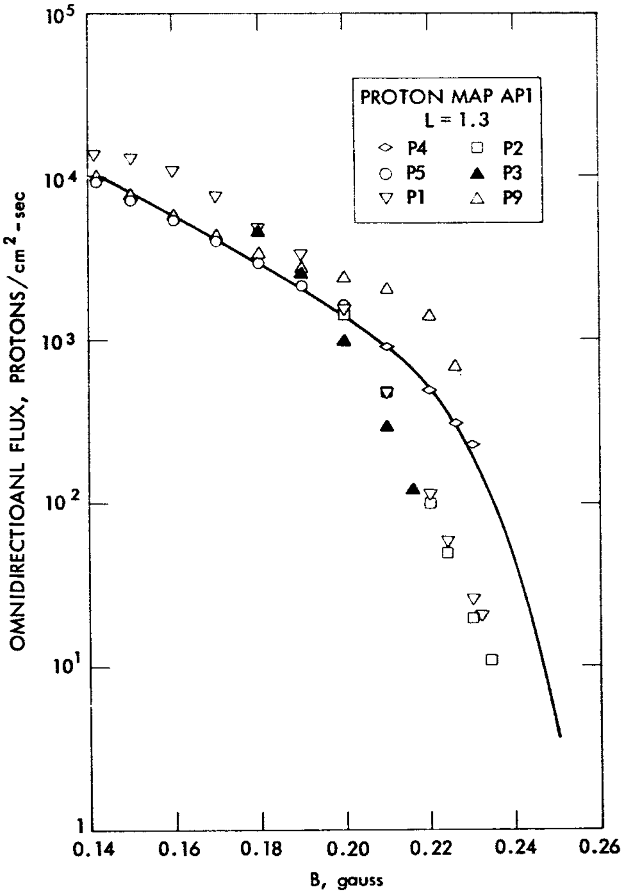

Figure 37—Comparison of proton map AP1 with experimental data at L = 1.3.

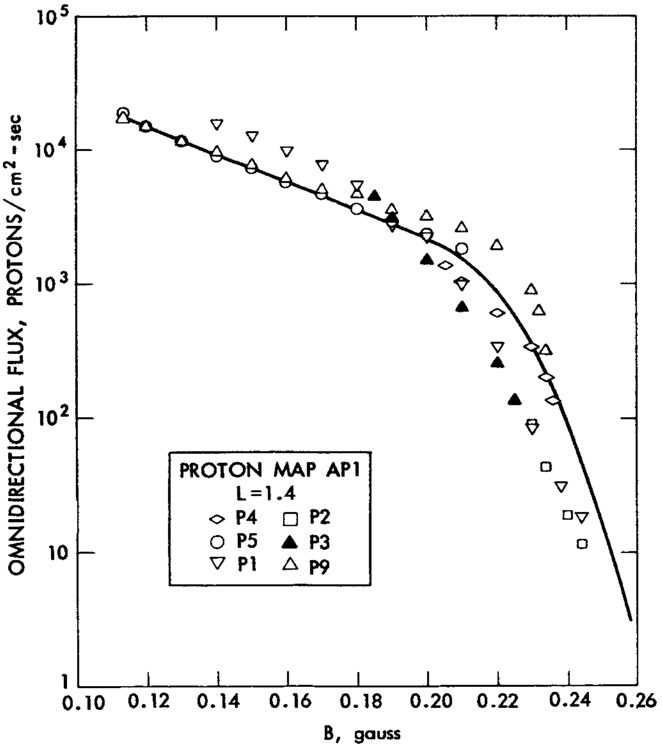

Figure 38—Comparison of proton map AP1 with experimental data at L = 1.4.

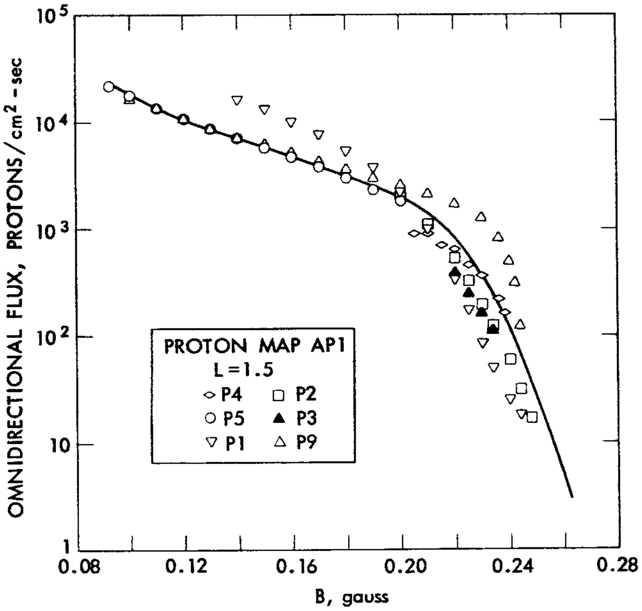

Figure 39—Comparison of proton map AP1 with experimental data at L = 1.5.

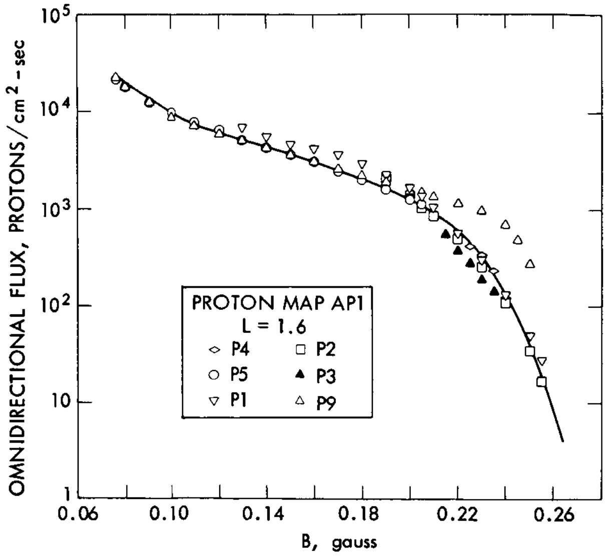

Figure 40—Comparison of proton map AP1 with experimental data at L = 1.6.

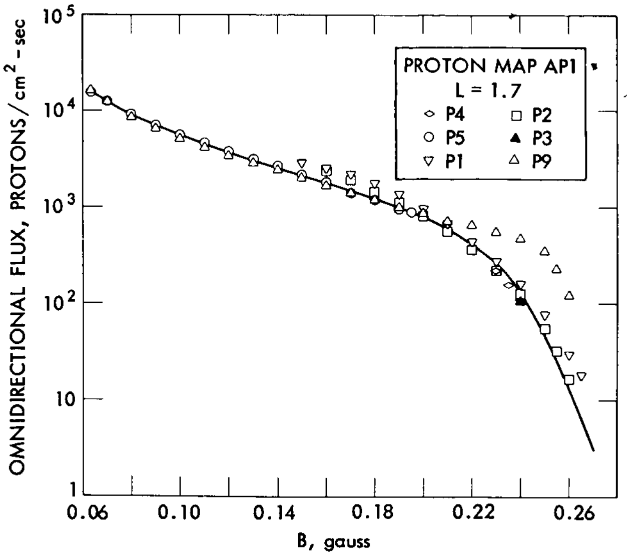

Figure 41—Comparison of proton map AP1 with experimental data at L = 1.7.

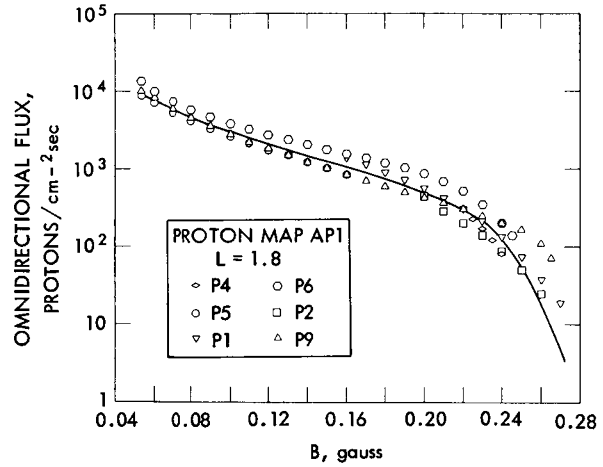

Figure 42—Comparison of proton map AP1 with experimental data at L = 1.8.

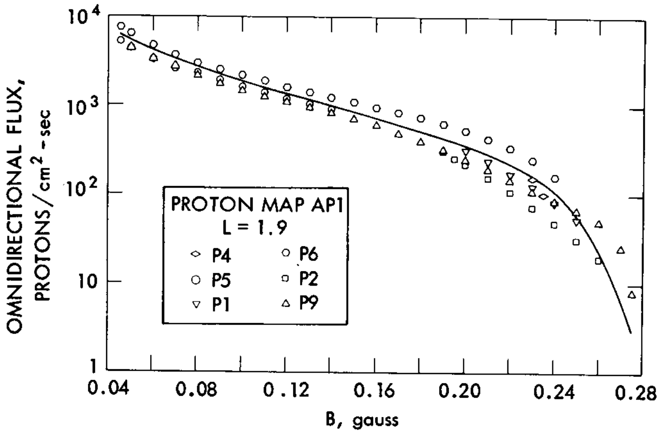

Figure 43—Comparison of proton map AP1 with experimental data at L = 1.9.

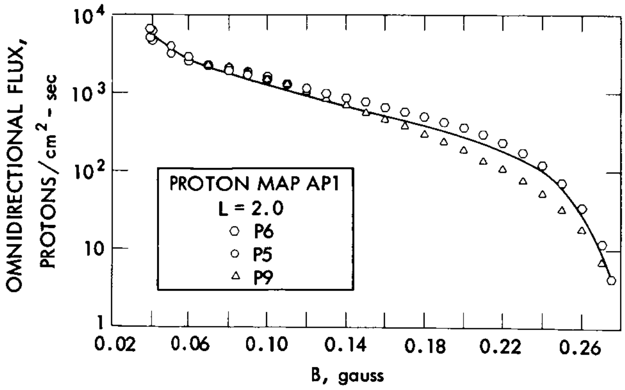

Figure 44—Comparison of proton map AP1 with experimental data at L = 2.0.

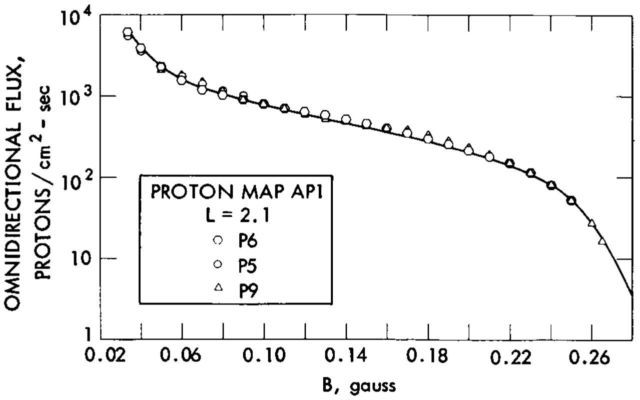

Figure 45—Comparison of proton map AP1 with experimental data at L = 2.1.

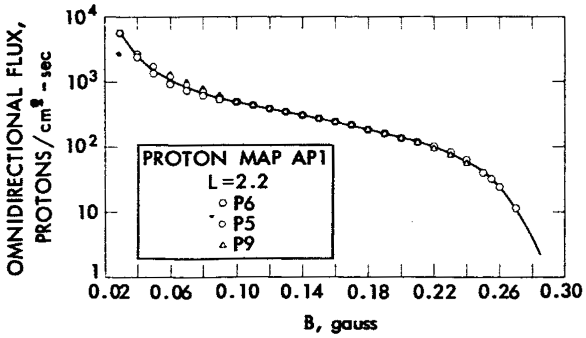

Figure 46—Comparison of proton map AP1 with experimental data at L = 2.2.

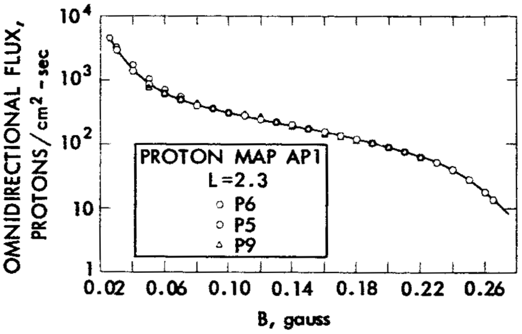

Figure 47—Comparison of proton map AP1 with experimental data at L = 2.3

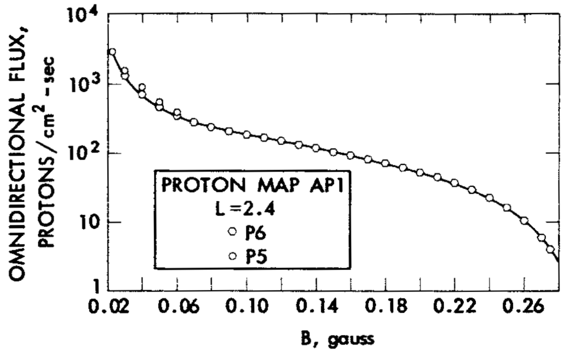

Figure 48—Comparison of proton map AP1 with experimental data at L = 2.4

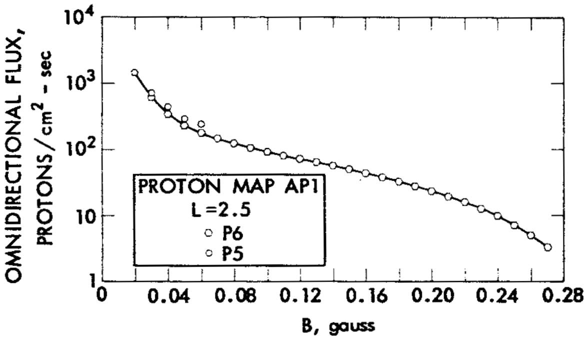

Figure 49—Comparison of proton map AP1 with experimental data at L = 2.5.

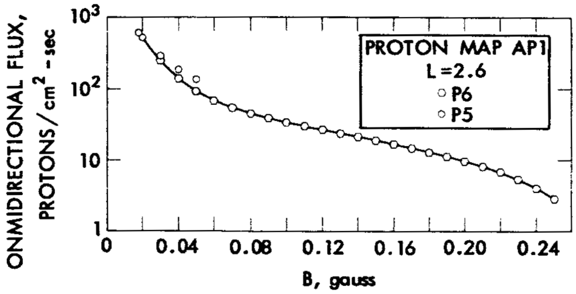

Figure 50—Comparison of proton map AP1 with experimental data at L = 2.6.

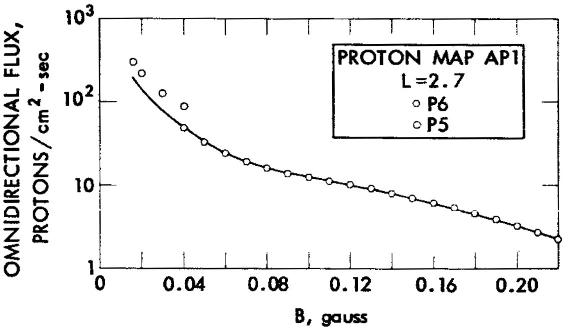

Figure 51—Comparison of proton map AP1 with experimental data at L = 2.7.

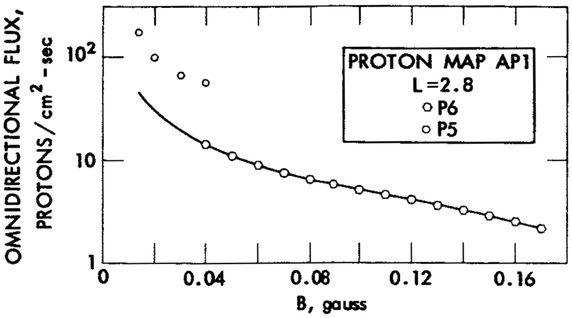

Figure 52—Comparison of proton map AP1 with experimental data at L = 2.8.

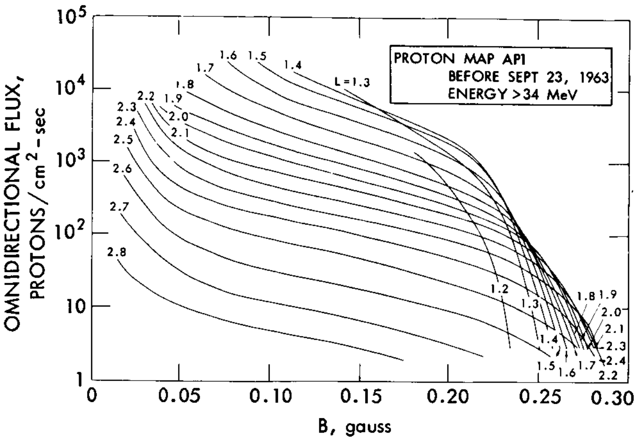

Figure 53—The flux versus B plot of AP1, E > 34 MeV.

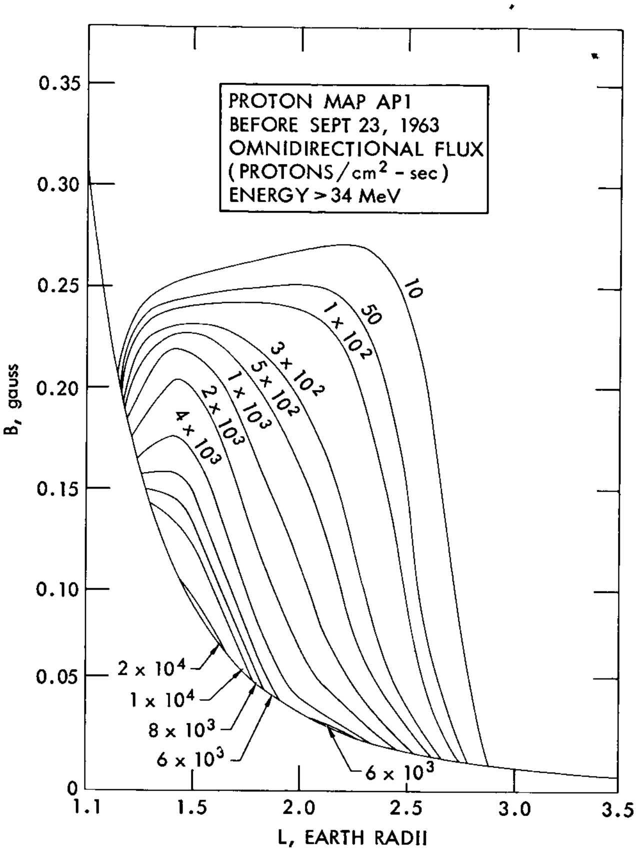

Figure 54—The B-L flux map for AP1. The contours are the omnidirectional flux above 34 MeV.

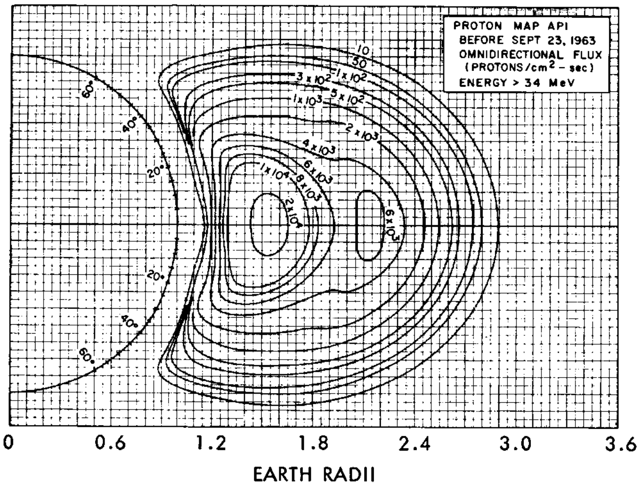

Figure 55—The R-λ flux map for AP1. The contours are the omnidirectional flux above 34 MeV.

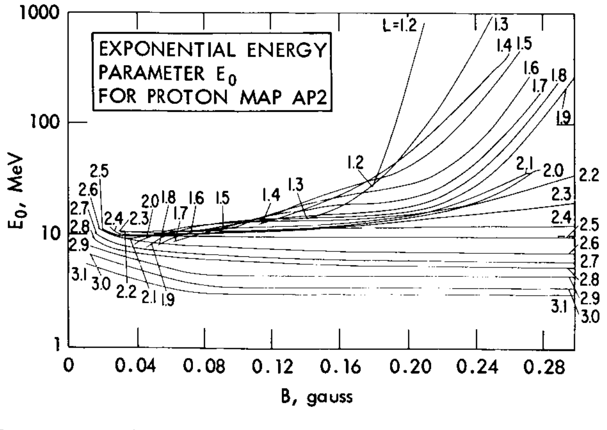

Figure 56—The energy spectral parameter, E_o, for proton map AP2. This function is to be used over the energy range 15 - 30 MeV.

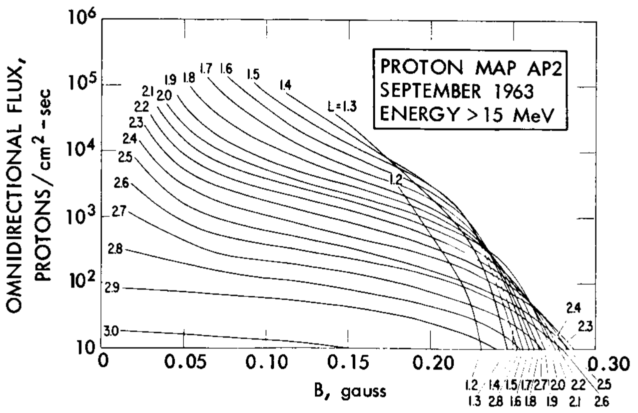

Figure 57—The flux versus B plot of AP2, E > 15 MeV.

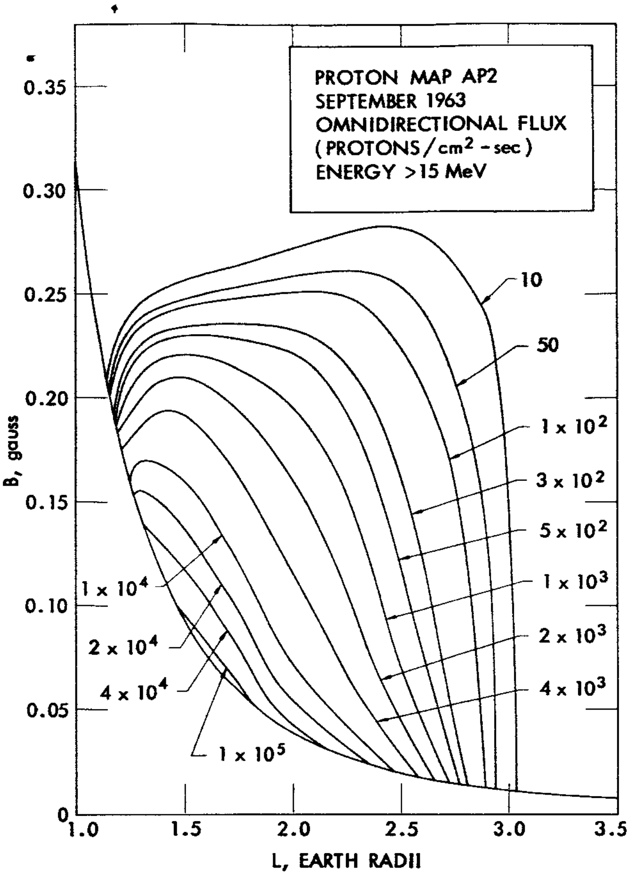

Figure 58—The B-L flux map for AP2. The contours are the omnidirectional flux above 15 MeV.

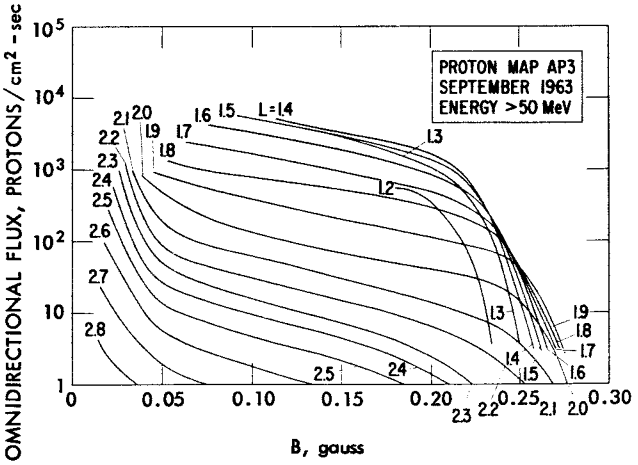

Figure 60—The flux versus B plot of AP3, E > 50 MeV.

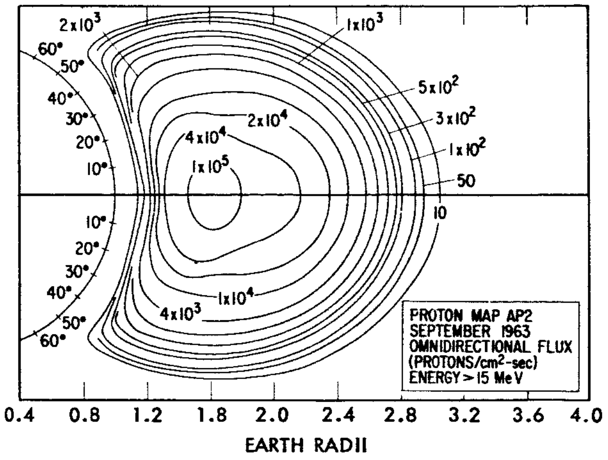

Figure 59—The R-λ flux map for AP2. The contours are the omnidirectional flux above 15 MeV.

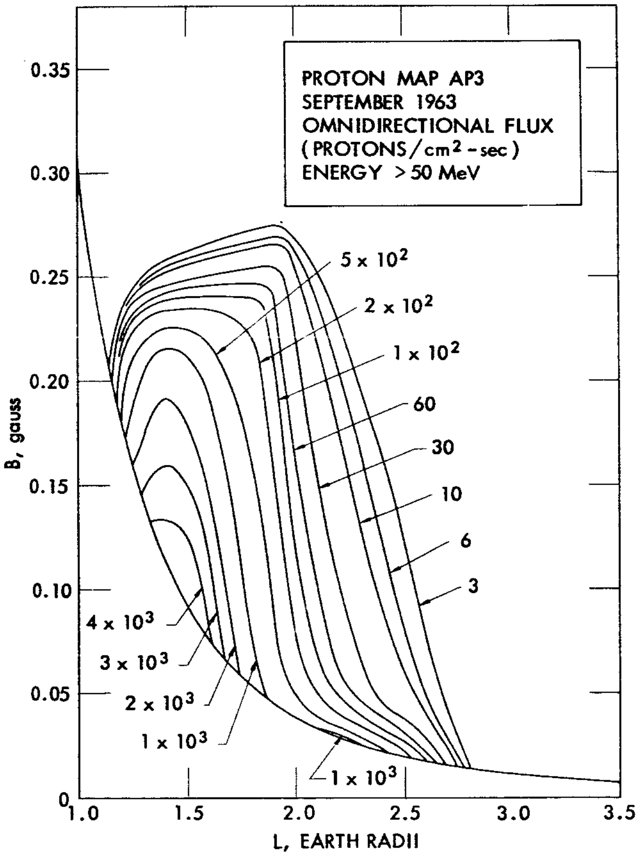

Figure 61—The B-L flux map for AP3. The contours are the omnidirectional flux above 50 MeV.

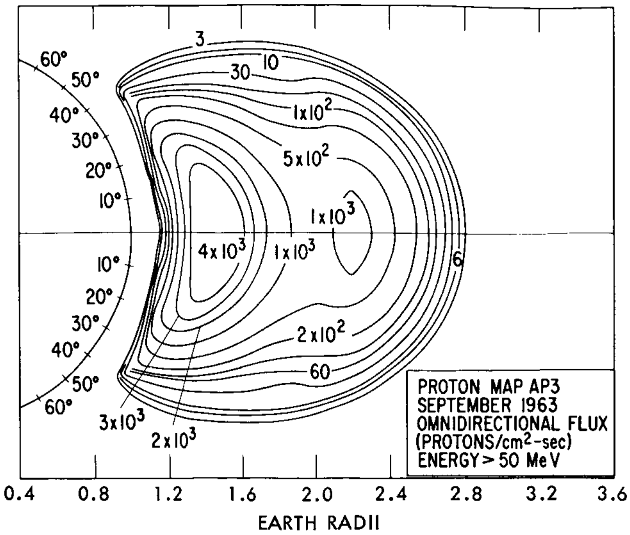

Figure 62—The R- λ flux map for AP3. The contours are the omnidirectional flux above 50 MeV.

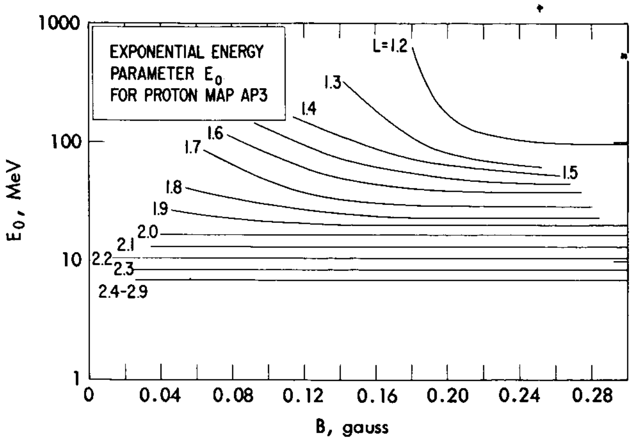

Figure 63—The energy spectral parameter, E_o, for proton map AP3. This function is to be used for energies greater than 50 MeV.

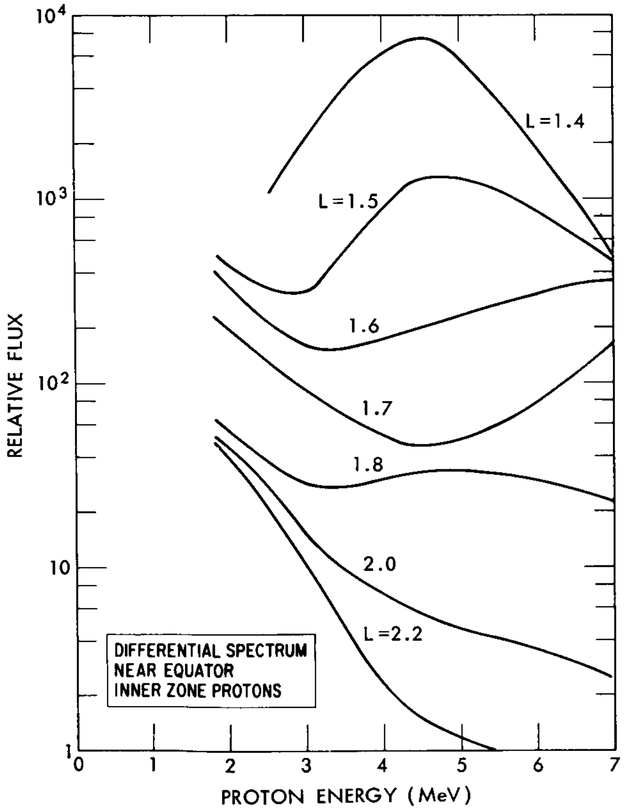

Figure 64—Differential proton spectrum near the equator for inner zone protons. This is estimated from Relay I and Explorer 15 measurements discussed in the text.

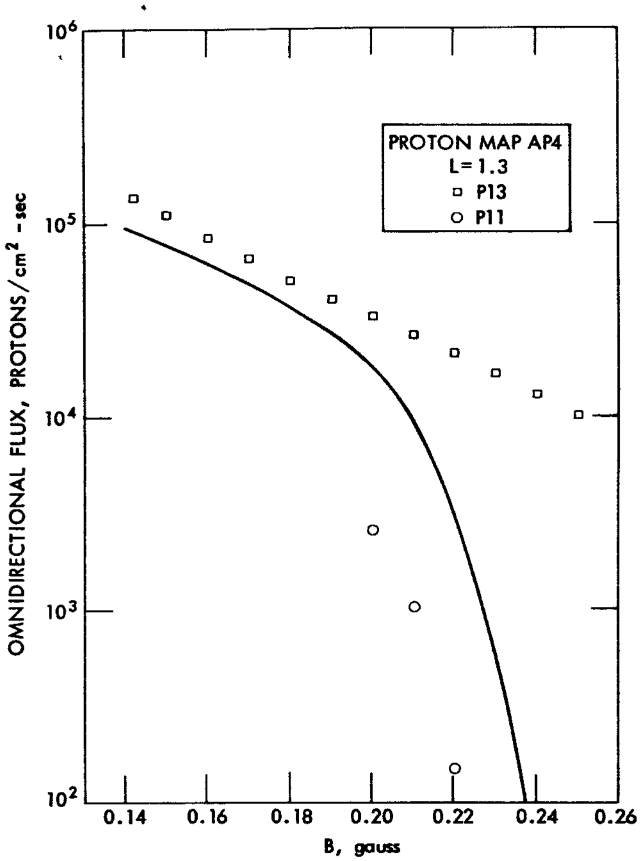

Figure 65—Comparison of proton map AP4 with experimental data at L = 1.3.

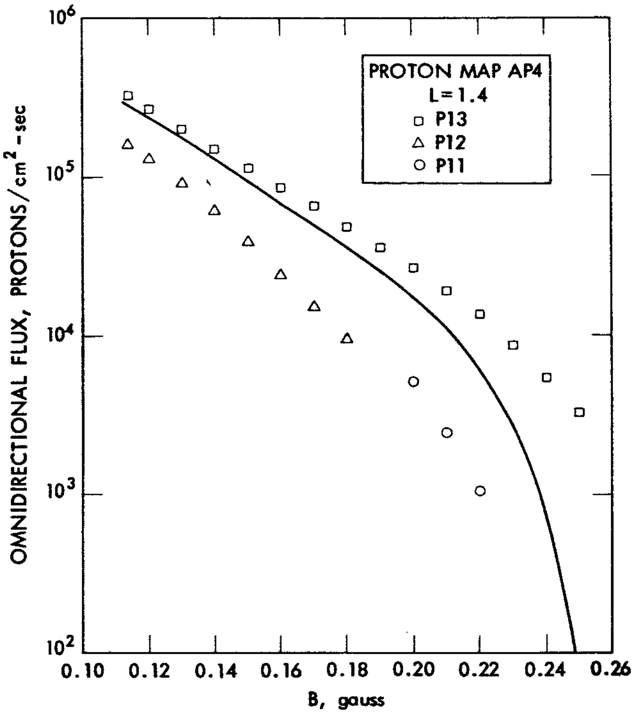

Figure 66—Comparison of proton map AP4 with experimental data at L = 1.4.

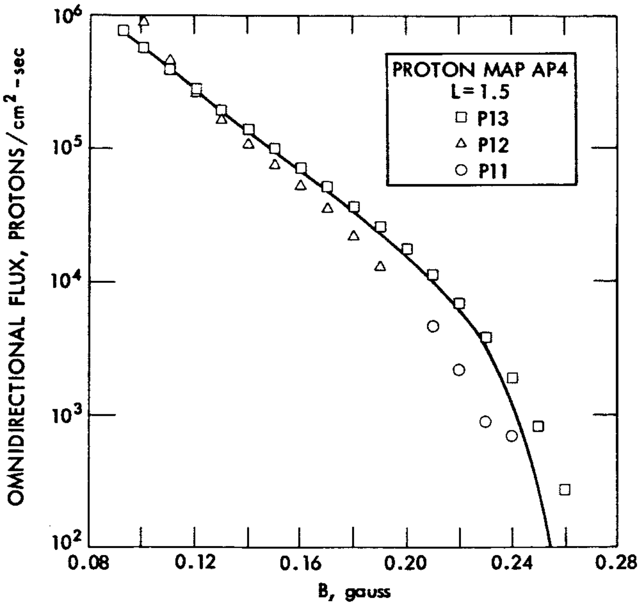

Figure 67—Comparison of proton map AP4 with experimental data at L = 1.5.

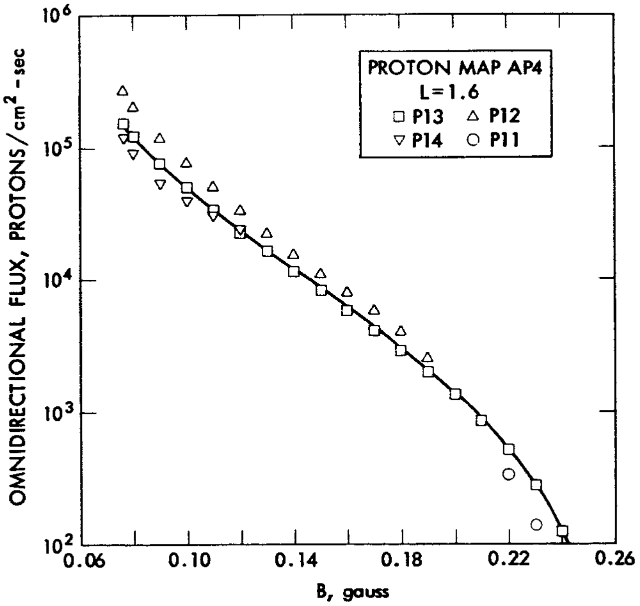

Figure 68—Comparison of proton map AP4 with experimental data at L = 1.6.

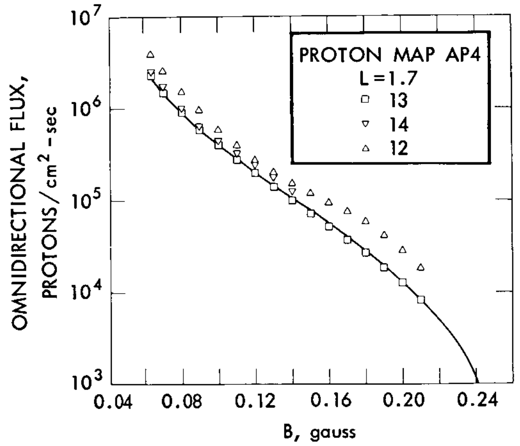

Figure 69—Comparison of proton map AP4 with experimental data at L = 1.7.

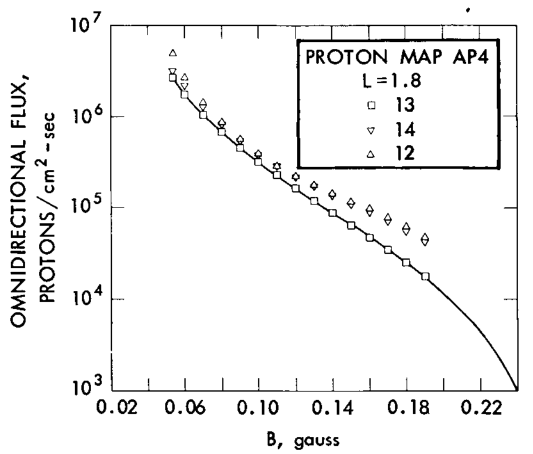

Figure 70—Comparison of proton map AP4 with experimental data at L = 1.8.

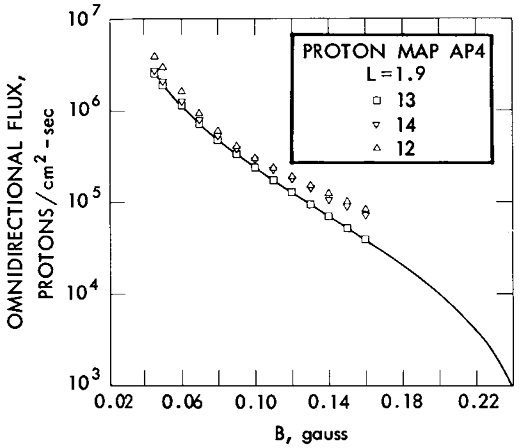

Figure 71—Comparison of proton map AP4 with experimental data at L = 1.9.

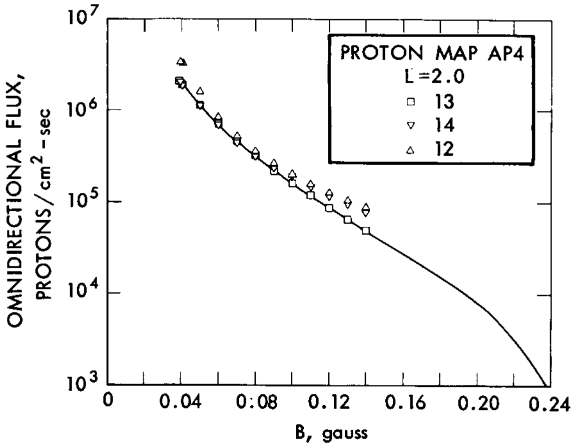

Figure 72—Comparison of proton map AP4 with experimental data at L = 2.0

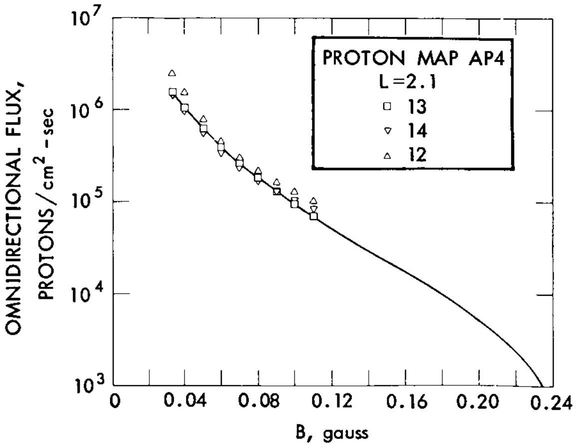

Figure 73—Comparison of proton map AP4 with experimental data at L = 2.1.

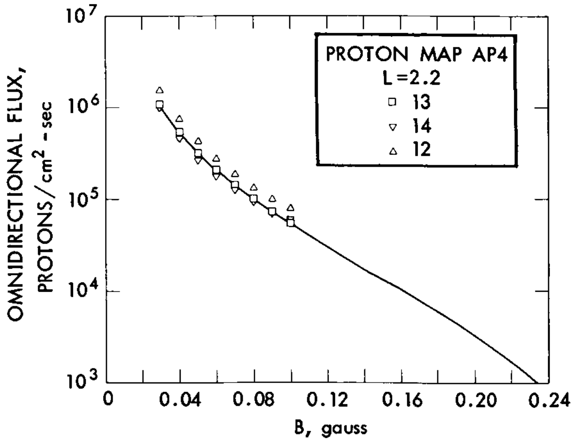

Figure 74—Comparison of proton map AP4 with experimental data at L = 2.2.

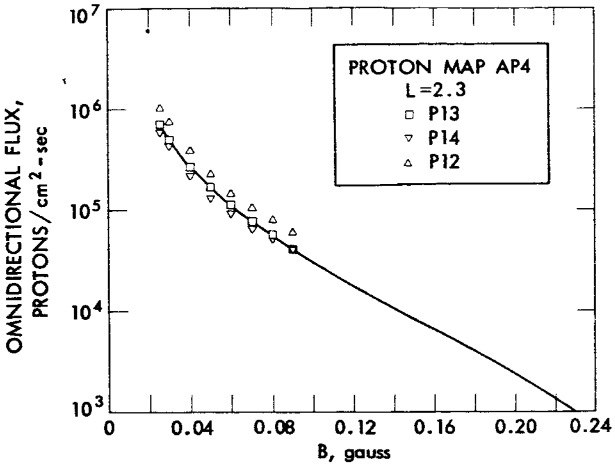

Figure 75—Comparison of proton map AP4 with experimental data at L = 2.3

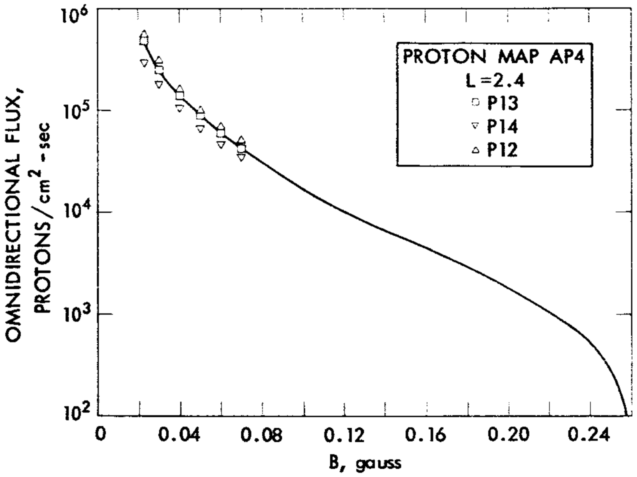

Figure 76—Comparison of proton map AP4 with experimental data at L = 2.4.

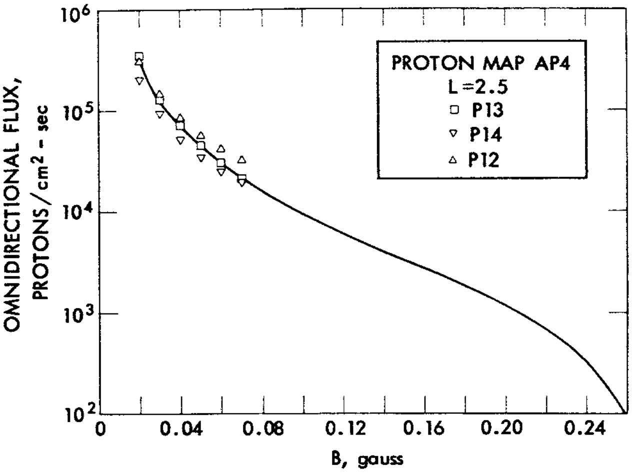

Figure 77—Comparison of proton map AP4 with experimental data at L = 2.5.

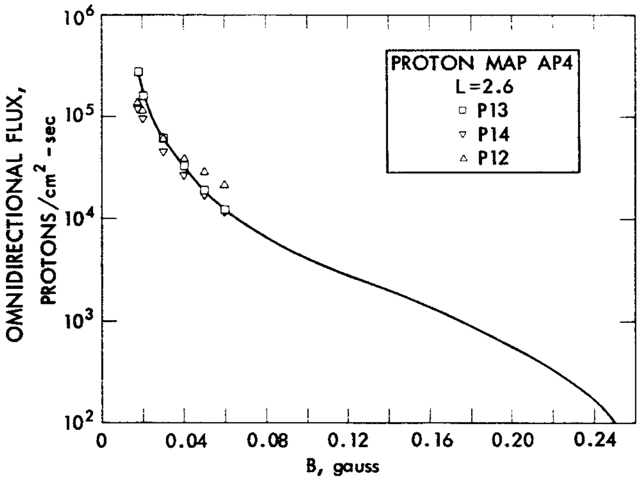

Figure 78—Comparison of proton map AP4 with experimental data at L = 2.6.

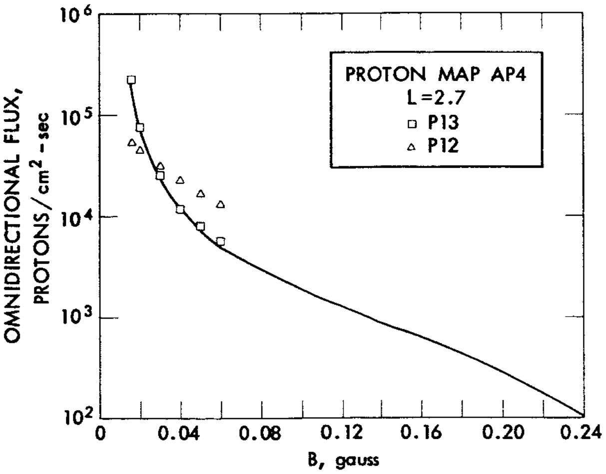

Figure 79—Comparison of proton map AP4 with experimental data at L = 2.7.

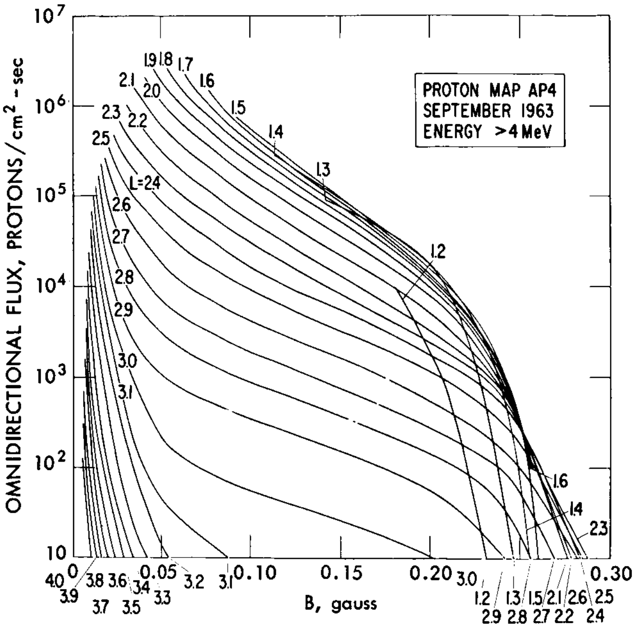

Figure 80—The flux versus B plot of AP4, E > 4 MeV.

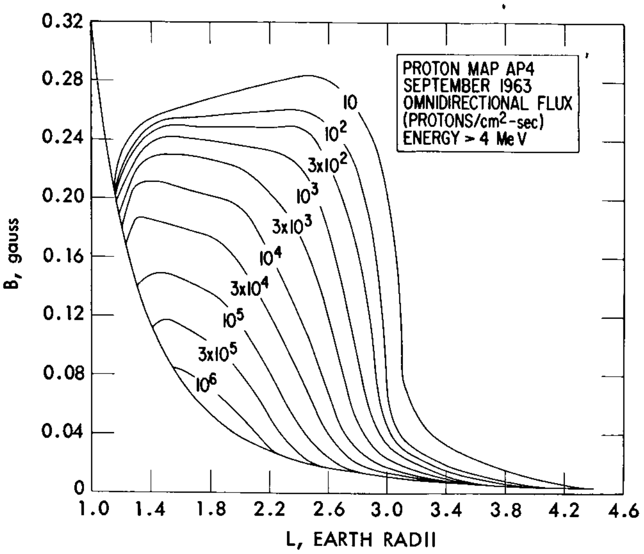

Figure 81—The B-L flux map for AP4. The contours are the omnidirectional flux above 4 MeV.

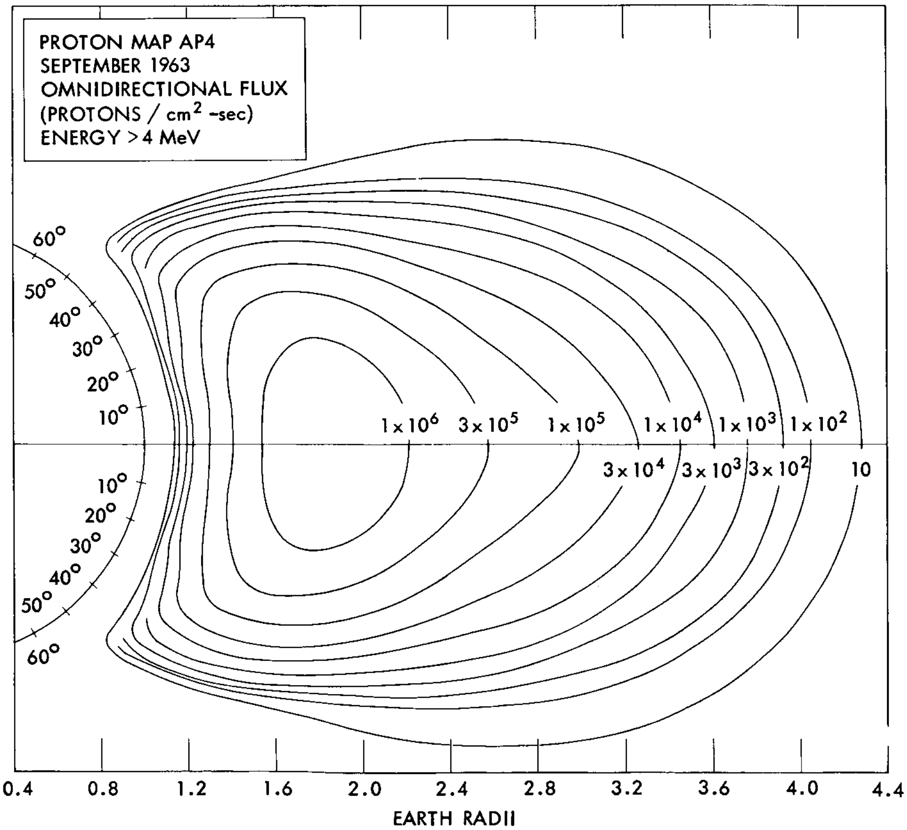

Figure 82—The R-λ flux map for AP4. The contours are the omnidirectional flux above 4 MeV.

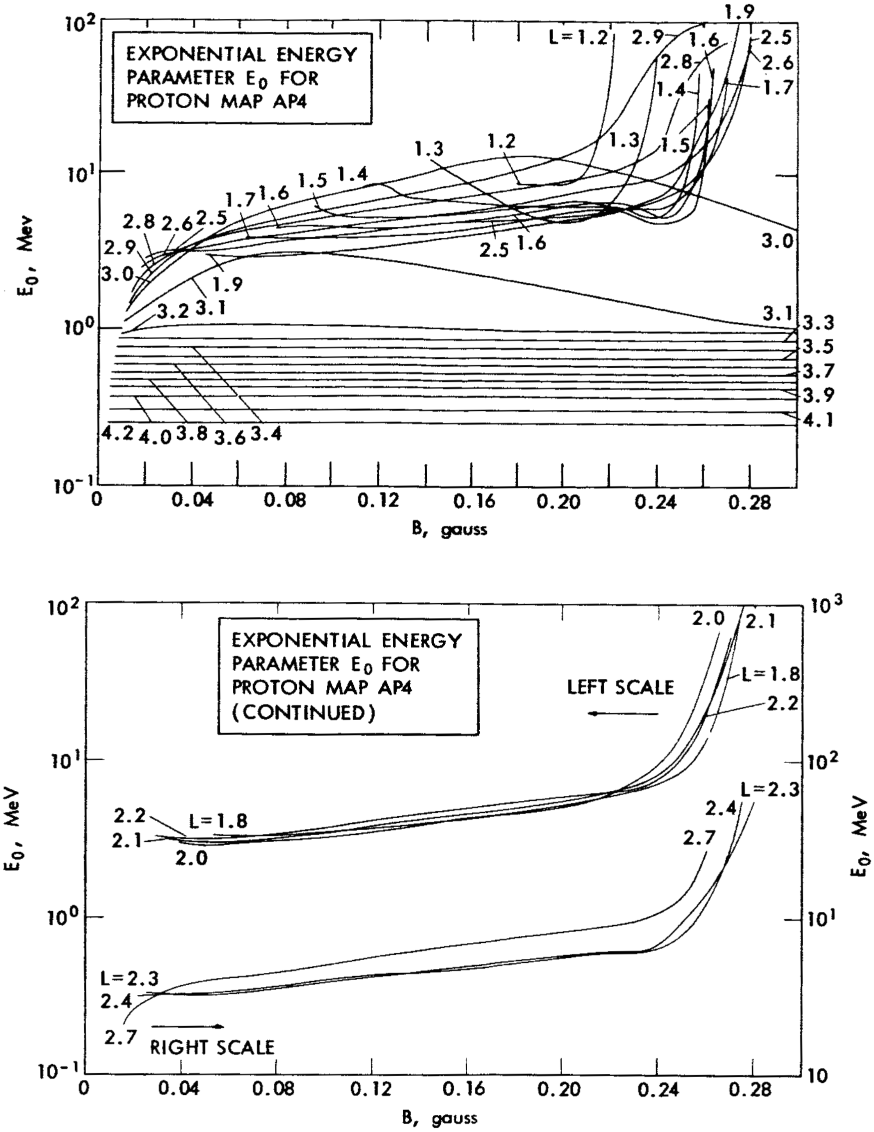

Figure 83—The energy spectral parameter, E_o, for proton map AP4. This function is to be used over the energy range 4 - 15 MeV.

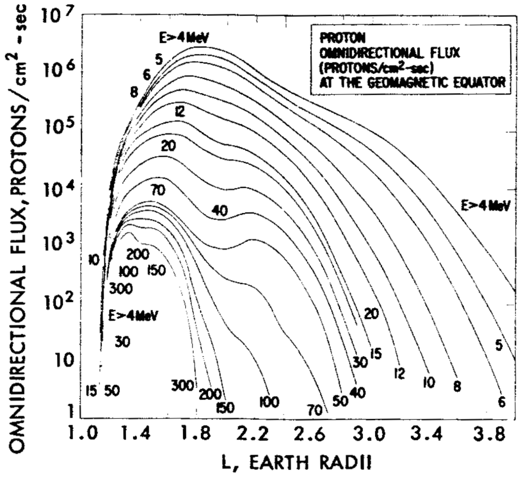

Figure 84—The omnidirectional proton flux at the geomagnetic equator. The curves have been calculated using the proton maps AP1-4 and the corresponding spectral functions.

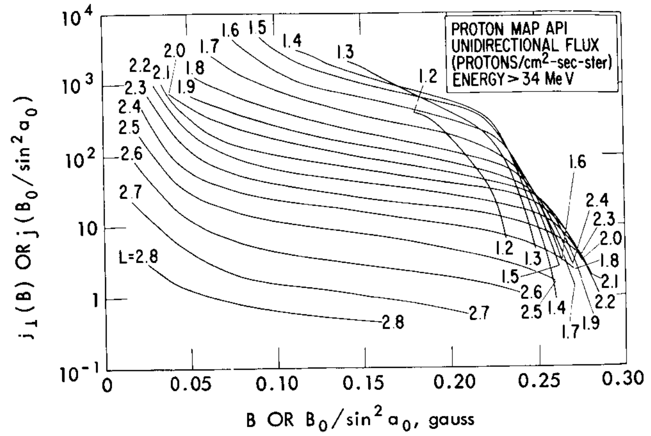

Figure 85—$j_\perp$ versus B for AP1, E > 34 MeV.

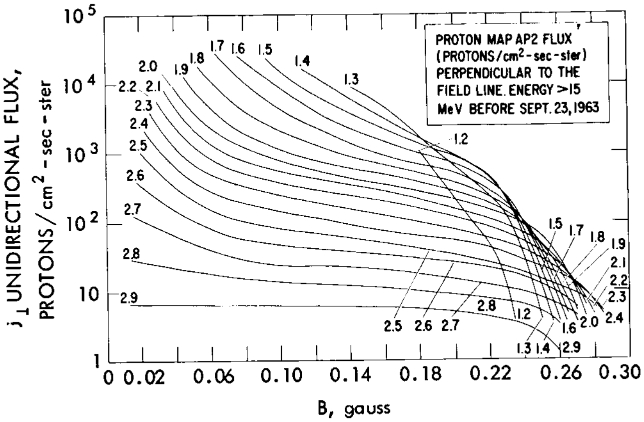

Figure 86—$j_\perp$ versus B for AP2, E > 15 MeV.

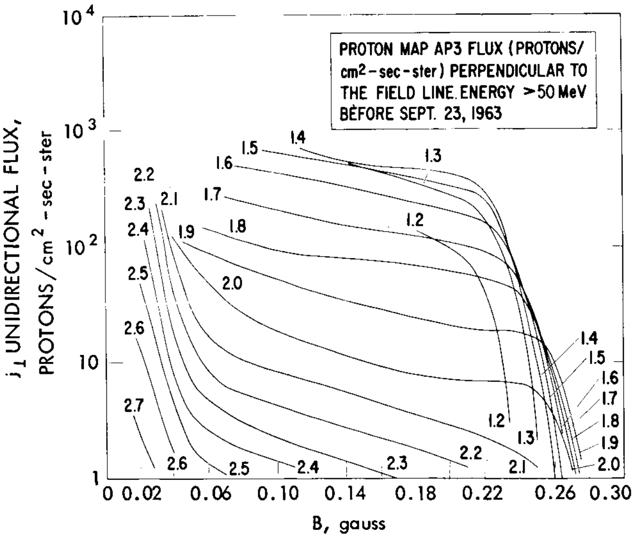

Figure 87—$j_\perp$ versus B for AP3, E > 50 MeV.

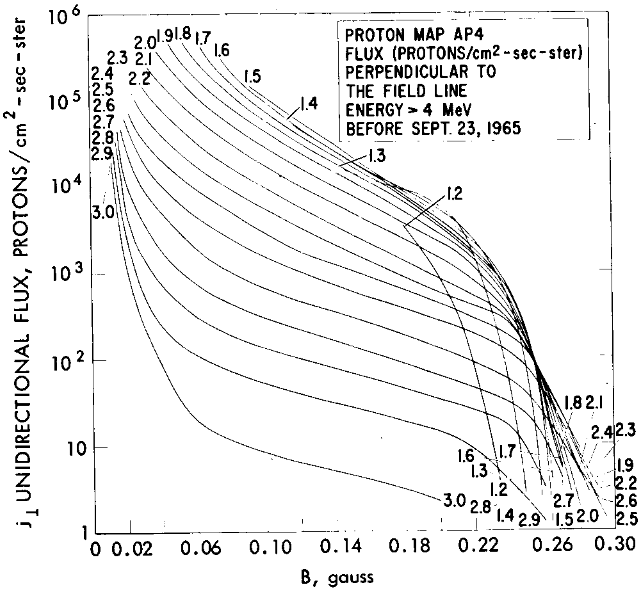

Figure 88—$j_\perp$ versus B for AP4, E > 4 MeV.

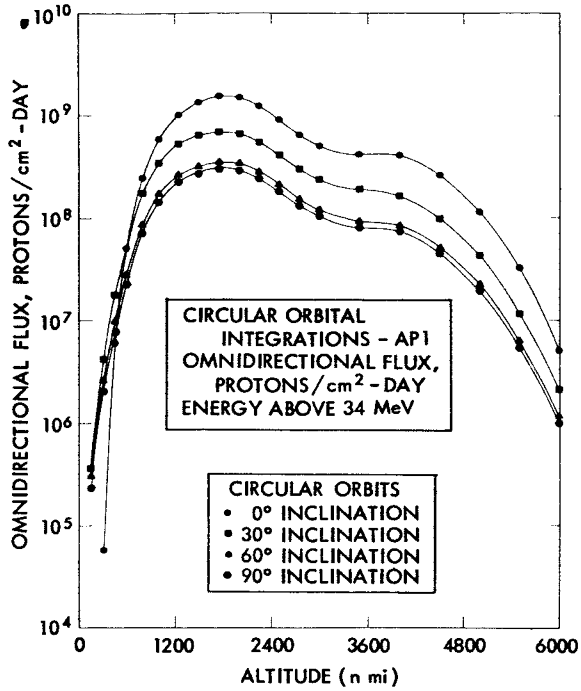

Figure 89—Orbital integrations with AP1, E > 34 MeV.

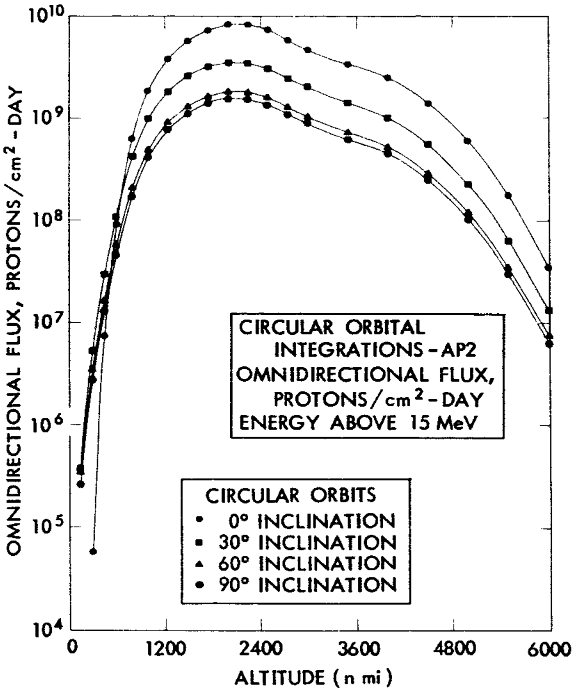

Figure 90—Orbital integrations with AP2, E > 15 MeV.

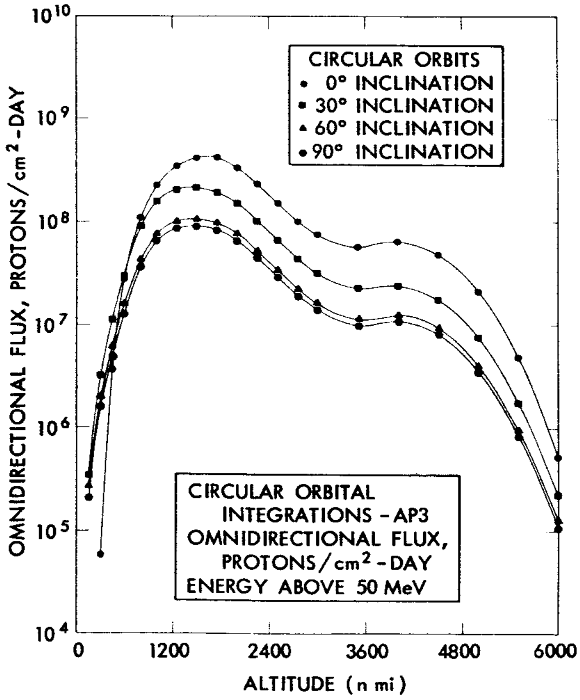

Figure 91—Orbital integrations with AP3, E > 50 MeV.

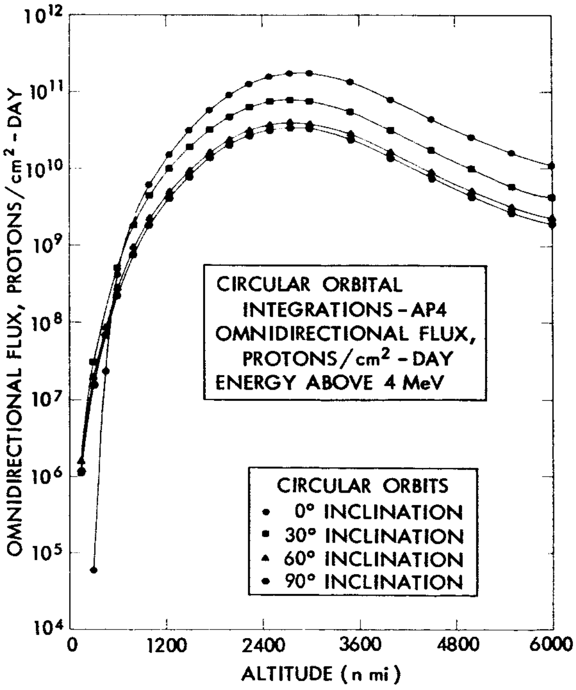

Figure 92—Orbital integrations with AP4, E > 4 MeV.

NASA-Langley, 1966

"The aeronautical and space activities of the United States shall be conducted so as to contribute . . . to the expansion of human knowledge of phenomena in the atmosphere and space. The Administration shall provide for the widest practicable and appropriate dissemination of information concerning its activities and the results thereof."

—NATIONAL AERONAUTICS AND SPACE ACT OF 1958

NASA SCIENTIFIC AND TECHNICAL PUBLICATIONS

TECHNICAL REPORTS: Scientific and technical information considered important, complete, and a lasting contribution to existing knowledge.

TECHNICAL NOTES: Information less broad in scope but nevertheless of importance as a contribution to existing knowledge.

TECHNICAL MEMORANDUMS: Information receiving limited distribution because of preliminary data, security classification, or other reasons.

CONTRACTOR REPORTS: Technical information generated in connection with a NASA contract or grant and released under NASA auspices.

TECHNICAL TRANSLATIONS: Information published in a foreign language considered to merit NASA distribution in English.

SPECIAL PUBLICATIONS: Information derived from or of value to NASA activities. Publications include conference proceedings, monographs, data compilations, handbooks, sourcebooks, and special bibliographies.

TECHNOLOGY UTILIZATION PUBLICATIONS: Information on technology used by NASA that may be of particular interest in commercial and other nonaerospace applications. Publications include Tech Briefs; Technology Utilization Reports and Notes; and Technology Surveys.

Details on the availability of these publications may be obtained from:

SCIENTIFIC AND TECHNICAL INFORMATION DIVISION
NATIONAL AERONAUTICS AND SPACE ADMINISTRATION
Washington, D.C. 20546

1612